



HAL
open science

TOI-1231 b: A Temperate, Neptune-sized Planet Transiting the Nearby M3 Dwarf NLTT 24399

Jennifer A Burt, Diana Dragomir, Paul Mollière, Allison Youngblood, Antonio García Muñoz, John Mccann, Laura Kreidberg, Chelsea X Huang, Karen A Collins, Jason D Eastman, et al.

► **To cite this version:**

Jennifer A Burt, Diana Dragomir, Paul Mollière, Allison Youngblood, Antonio García Muñoz, et al.. TOI-1231 b: A Temperate, Neptune-sized Planet Transiting the Nearby M3 Dwarf NLTT 24399. *The Astronomical Journal*, 2021, 162 (3), pp.87. 10.3847/1538-3881/ac0432 . hal-03378247

HAL Id: hal-03378247

<https://hal.science/hal-03378247>

Submitted on 14 Oct 2021

HAL is a multi-disciplinary open access archive for the deposit and dissemination of scientific research documents, whether they are published or not. The documents may come from teaching and research institutions in France or abroad, or from public or private research centers.

L'archive ouverte pluridisciplinaire **HAL**, est destinée au dépôt et à la diffusion de documents scientifiques de niveau recherche, publiés ou non, émanant des établissements d'enseignement et de recherche français ou étrangers, des laboratoires publics ou privés.

TOI-1231 b: A Temperate, Neptune-Sized Planet Transiting the Nearby M3 Dwarf NLTT 24399

JENNIFER A. BURT,¹ DIANA DRAGOMIR,² PAUL MOLLIÈRE,³ ALLISON YOUNGBLOOD,⁴ ANTONIO GARCÍA MUÑOZ,⁵
JOHN MCCANN,⁶ LAURA KREIDBERG,³ CHELSEA X. HUANG,^{7,*} KAREN A. COLLINS,⁸ JASON D. EASTMAN,⁸ LYU ABE,⁹
JOSE M. ALMENARA,¹⁰ IAN J. M. CROSSFIELD,¹¹ CARL ZIEGLER,¹² JOSEPH E. RODRIGUEZ,^{8,13} ERIC E. MAMAJEK,¹
KEIVAN G. STASSUN,^{14,15} SAMUEL P. HALVERSON,¹ STEVEN JR. VILLANUEVA,^{7,†} R. PAUL BUTLER,¹⁶
SHARON XUESONG WANG,^{17,18} RICHARD P. SCHWARZ,¹⁹ GEORGE R. RICKER,⁷ ROLAND VANDERSPEK,⁷ DAVID W. LATHAM,⁸
S. SEAGER,^{7,20,21} JOSHUA N. WINN,²² JON M. JENKINS,²³ ABDELKRIM AGABI,⁹ XAVIER BONFILS,¹⁰ DAVID CIARDI,²⁴
MARION COINTEPAS,^{10,25} JEFFREY D. CRANE,¹⁷ NICOLAS CROUZET,²⁶ GEORGINA DRANSFIELD,²⁷ FABO FENG,^{28,29}
ELISE FURLAN,²⁴ TRISTAN GUILLOT,⁹ ARVIND F. GUPTA,^{30,31} STEVE B. HOWELL,²³ ERIC L. N. JENSEN,³² NICHOLAS LAW,³³
ANDREW W. MANN,³³ WENCESLAS MARIE-SAINTE,³⁴ RACHEL A. MATSON,³⁵ ELISABETH C. MATTHEWS,³⁶
DJAMEL MÉKARNIA,⁹ JOSHUA PEPPER,³⁷ NIC SCOTT,²³ STEPHEN A. SHECTMAN,¹⁷ JOSHUA E. SCHLIEDER,³⁸
FRANÇOIS-XAVIER SCHMIDER,⁹ DANIEL J. STEVENS,^{39,40,‡} JOHANNA K. TESKE,¹⁶ AMAURY H.M.J. TRIAUD,²⁷
DAVID CHARBONNEAU,⁸ ZACHORY K. BERTA-THOMPSON,⁴¹ CHRISTOPHER J. BURKE,⁷ TANSU DAYLAN,^{7,§}
THOMAS BARCLAY,^{42,43} BILL WOHLER,^{44,23} AND C. E. BRASSEUR⁴⁵

¹Jet Propulsion Laboratory, California Institute of Technology, 4800 Oak Grove Drive, Pasadena, CA 91109, USA

²Department of Physics and Astronomy, University of New Mexico, 1919 Lomas Blvd NE, Albuquerque, NM 87131, USA

³Max-Planck-Institut für Astronomie, Königstuhl 17, 69117, Heidelberg, Germany

⁴Laboratory for Atmospheric and Space Physics, 1234 Innovation Drive, Boulder, CO, 80303, USA

⁵AIM, CEA, CNRS, Université Paris-Saclay, Université de Paris, Gif-sur-Yvette, France.

⁶Department of Physics, University of California, Santa Barbara, CA 93106, USA

⁷Department of Physics and Kavli Institute for Astrophysics and Space Research, Massachusetts Institute of Technology, Cambridge, MA 02139, USA

⁸Center for Astrophysics | Harvard & Smithsonian, 60 Garden Street, Cambridge, MA 02138, USA

⁹Université Côte d'Azur, Observatoire de la Côte d'Azur, CNRS, Laboratoire Lagrange, Bd de l'Observatoire, CS 34229, 06304 Nice cedex 4, France

¹⁰Univ. Grenoble Alpes, CNRS, IPAG, 38000, Grenoble, France

¹¹Physics & Astronomy Department, University of Kansas, Lawrence, KS, USA

¹²Dunlap Institute for Astronomy and Astrophysics, University of Toronto, 50 St. George Street, Toronto, Ontario M5S 3H4, Canada

¹³Department of Physics and Astronomy, Michigan State University, East Lansing, MI, 48824 USA

¹⁴Department of Physics and Astronomy, Vanderbilt University, Nashville, TN 37235, USA

¹⁵Department of Physics, Fisk University, Nashville, TN 37208, USA

¹⁶Earth & Planets Laboratory, Carnegie Institution for Science, 5241 Broad Branch Road, NW, Washington, DC 20015, USA

¹⁷The Observatories of the Carnegie Institution for Science, 813 Santa Barbara Street, Pasadena, CA 91101, USA

¹⁸Department of Astronomy, Tsinghua University, Beijing 100084, People's Republic of China

¹⁹Patashnick Voorheesville Observatory, Voorheesville, NY 12186, USA

²⁰Department of Earth, Atmospheric and Planetary Sciences, Massachusetts Institute of Technology, Cambridge, MA 02139, USA

²¹Department of Aeronautics and Astronautics, MIT, 77 Massachusetts Avenue, Cambridge, MA 02139, USA

²²Department of Astrophysical Sciences, Princeton University, 4 Ivy Lane, Princeton, NJ 08544, USA

²³NASA Ames Research Center, Moffett Field, CA 94035, USA

²⁴NASA Exoplanet Science Institute, Infrared Processing & Analysis Center, Jet Propulsion Laboratory, California Institute of Technology, Pasadena CA 91125, USA

²⁵Observatoire de l'Université de Genève, Chemin des Maillettes 51, 1290 Versoix, Switzerland

²⁶European Space Agency (ESA), European Space Research and Technology Centre (ESTEC), Keplerlaan 1, 2201 AZ Noordwijk, The Netherlands

²⁷School of Physics & Astronomy, University of Birmingham, Edgbaston, Birmingham, B15 2TT, UK

²⁸Tsung-Dao Lee Institute, Shanghai Jiao Tong University, 800 Dongchuan Road, Shanghai 200240, People's Republic of China

²⁹Department of Astronomy, School of Physics and Astronomy, Shanghai Jiao Tong University, 800 Dongchuan Road, Shanghai 200240, People's Republic of China

³⁰Department of Astronomy & Astrophysics, 525 Davey Laboratory, The Pennsylvania State University, University Park, PA, 16802, USA

³¹Center for Exoplanets and Habitable Worlds, 525 Davey Laboratory, The Pennsylvania State University, University Park, PA, 16802, USA

³²Dept. of Physics & Astronomy, Swarthmore College, Swarthmore PA 19081, USA

³³Department of Physics and Astronomy, The University of North Carolina at Chapel Hill, Chapel Hill, NC 27599-3255, USA

³⁴Concordia Station, IPEV/PNRA, Antarctica

³⁵U.S. Naval Observatory, Washington, DC 20392, USA

³⁶Observatoire de l'Université de Genève, Chemin des Maillettes 51, 1290 Versoix, Switzerland

³⁷Department of Physics, Lehigh University, 16 Memorial Drive East, Bethlehem, PA 18015, USA

³⁸Exoplanets and Stellar Astrophysics Laboratory, Code 667, NASA Goddard Space Flight Center, Greenbelt, MD, 20771, USA

³⁹Department of Astronomy & Astrophysics, The Pennsylvania State University, 525 Davey Lab, University Park, PA 16802, USA

⁴⁰Center for Exoplanets and Habitable Worlds, The Pennsylvania State University, 525 Davey Lab, University Park, PA 16802, USA

⁴¹University of Colorado Boulder, Boulder, CO 80309, USA

⁴²NASA Goddard Space Flight Center, 8800 Greenbelt Road, Greenbelt, MD 20771, USA

⁴³University of Maryland, Baltimore County, 1000 Hilltop Circle, Baltimore, MD 21250, USA

⁴⁴SETI Institute, Mountain View, CA 94043, USA

⁴⁵Space Telescope Science Institute

ABSTRACT

We report the discovery of a transiting, temperate, Neptune-sized exoplanet orbiting the nearby ($d = 27.5$ pc), M3V star TOI-1231 (NLTT 24399, L 248-27, 2MASS J10265947-5228099). The planet was detected using photometric data from the *Transiting Exoplanet Survey Satellite* and followed up with observations from the Las Cumbres Observatory and the Antarctica Search for Transiting ExoPlanets program. Combining the photometric data sets, we find that the newly discovered planet has a radius of $3.65^{+0.16}_{-0.15} R_{\oplus}$, and an orbital period of 24.246 days. Radial velocity measurements obtained with the Planet Finder Spectrograph on the Magellan Clay telescope confirm the existence of the planet and lead to a mass measurement of $15.5 \pm 3.3 M_{\oplus}$. With an equilibrium temperature of just 330K TOI-1231 b is one of the coolest small planets accessible for atmospheric studies thus far, and its host star's bright NIR brightness ($J=8.88$, $K_s=8.07$) make it an exciting target for HST and JWST. Future atmospheric observations would enable the first comparative planetology efforts in the 250-350 K temperature regime via comparisons with K2-18 b. Furthermore, TOI-1231's high systemic radial velocity (70.5 km s^{-1}) may allow for the detection of low-velocity hydrogen atoms escaping the planet by Doppler shifting the H I Ly-alpha stellar emission away from the geocoronal and ISM absorption features.

Keywords: Exoplanets (498), Planetary system formation (1257), Radial velocity (1332), Transit photometry (1709)

1. INTRODUCTION

The observing strategy adopted by NASA's Transiting Exoplanet Survey Satellite (*TESS*, Ricker et al. 2014), wherein each hemisphere is divided into 13 sectors each of which is surveyed for roughly 28 days, is producing the most comprehensive all-sky search for transiting planets. This approach has already proven its capability to detect both large and small planets (Wang et al. 2019; Rodriguez et al. 2019; Dragomir et al. 2019; Luque et al. 2019; Burt et al. 2020) around stars ranging from Sun-like (Huang et al. 2018) down to low-mass M dwarf stars (Vanderspek et al. 2019).

Although it enables the detection of exoplanets across the sky, *TESS*'s survey strategy also produces significant

observational biases based on orbital period. Exoplanets must transit their host stars at least twice within *TESS*'s observing span in order to be detected with the correct period by the Science Processing Operations Center (SPOC) pipeline, which searches the 2-minute cadence *TESS* data obtained for pre-selected target stars (Jenkins et al. 2016a). Because 74% of *TESS*' total sky coverage is only observed for ≤ 28 days, the majority of *TESS* exoplanets detected by the SPOC are expected to have periods less than 14 days. Simulations of the *TESS* exoplanet yield presented in Sullivan et al. (2015) find mean and median orbital periods of 13.48 and 8.19 days, respectively, among all detected planets. Similarly, Barclay et al. (2018) found mean and median periods of 10.23 and 7.03 days among the full set of detected planets, and those values drop to just 7.42 and 5.89 days when considering the stars only observed during a single *TESS* sector. And additional simulations from Jiang et al. (2019) show that for stars observed only in a single sector the expected mean value of the most frequently

* Juan Carlos Torres Fellow

† Pappalardo Fellow

‡ Eberly Research Fellow

§ Kavli Fellow

detected orbital period is 5.01 days, with a most detected range of 2.12 to 11.82 days. Even when considering the Ecliptic poles, where *TESS* carries out 351 days of observing coverage during its primary mission, the expected mean orbital period is still only 10.93 days with a most detected range from 3.35 to 35.65 days.

Of the 1994 *TESS* objects of interest (TOIs) identified as planet candidates using Sectors 1-26 of the primary mission, only $\sim 14\%$ have periods longer than 14 days¹. But these longer period (and thereby cooler) candidates are some of the most intriguing targets for atmospheric characterization. This is especially true for Neptune sized planets whose lower temperatures could spark several marked changes in the expected atmospheric chemistry: disequilibrium due to rain out is relevant, water clouds may form, and ammonia is the dominant carrier of nitrogen (see, e.g. Morley et al. 2014). Thus these cooler TOIs merit additional attention and focused follow up efforts both to confirm their planetary nature and to obtain the precise mass measurements necessary for correct interpretation of future transmission spectroscopy observations (Batalha et al. 2019).

Here we report the discovery of a Neptune-sized planet transiting TOI-1231 (NLTT 24399, L 248-27, TIC 447061717, 2MASS J10265947-5228099), a $V = 12.3$ mag M3V star (Gaidos et al. 2014) in the Vela constellation at $d = 27.493 \pm 0.0123$ pc ($\varpi = 36.3726 \pm 0.0163$ mas; GaiaEDR3 van Leeuwen et al. 2021). This paper is organized as follows. In Section 2 we characterize the host star using details from published catalogs and new data obtained once the *TESS* planet candidate was identified. In Section 3 we describe the initial discovery of TOI-1231 b and the follow up data obtained in an effort to characterize the planet. In Section 4 we outline the procedure used to perform a joint fit to the host star and planet, and then in Section 5 we conclude with a discussion of the planet’s promising potential for future atmospheric characterization.

2. STELLAR DATA & CHARACTERIZATION

2.1. Background

TOI-1231 was first reported as a high proper motion star ($0'35$ yr⁻¹) by Luyten (1957, as LTT 3840 and L 248-27), and later in the Revised NLTT catalog (Luyten 1979, as NLTT 24399). Over the past decade, the star has appeared in several surveys of high proper motion 2MASS and WISE stars and nearby M dwarfs (e.g. Lépine & Gaidos 2011; Frith et al. 2013; Kirk-

patrick et al. 2014; Schneider et al. 2016). The only previous spectral characterization of TOI-1231 was by Gaidos et al. (2014) in the CONCH-SHELL survey, who reported a spectral type of M3V. Previous estimates of the basic stellar parameters were reported by Gaidos et al. (2014); Muirhead et al. (2018); Stassun et al. (2019).

Table 1. Astrometry & Photometry for TOI-1231

Parameter	Value	Source
Designations	TIC 447061717 NLTT 24399	Stassun et al. (2019) Luyten (1979)
RA (ICRS, J2000)	10:26:59.34	Gaia EDR3
Dec (ICRS, J2000)	-52 28 04.16	Gaia EDR3
μ RA (mas yr ⁻¹)	-89.394 ± 0.019	Gaia EDR3
μ Dec (mas yr ⁻¹)	361.546 ± 0.015	Gaia EDR3
Parallax (mas)	36.3726 ± 0.0163	Gaia EDR3 ^a
Distance (pc)	27.4932 ± 0.0123	Gaia EDR3 ^a
v_R (km s ⁻¹)	70.48 ± 0.54	Gaia DR2
SpT	M3V	Gaidos et al. (2014)
<i>B</i>	13.739 ± 0.028	APASS/DR10
<i>V</i>	12.322 ± 0.023	APASS/DR10
<i>g'</i>	12.997 ± 0.044	APASS/DR10
<i>r'</i>	11.806 ± 0.070	APASS/DR10
<i>i'</i>	10.754 ± 0.175	APASS/DR10
<i>TESS</i>	10.2565 ± 0.007	TIC8
<i>G</i>	11.3612 ± 0.0009	Gaia EDR3
<i>G_{BP}</i>	12.5440 ± 0.0022	Gaia EDR3
<i>G_{RP}</i>	10.2735 ± 0.0015	Gaia EDR3
<i>J</i>	8.876 ± 0.027	2MASS
<i>H</i>	8.285 ± 0.038	2MASS
<i>K_s</i>	8.069 ± 0.026	2MASS
<i>W₁</i>	7.922 ± 0.024	WISE
<i>W₂</i>	7.826 ± 0.020	WISE
<i>W₃</i>	7.732 ± 0.017	WISE
<i>W₄</i>	7.515 ± 0.091	WISE
U (km s ⁻¹)	-20.25 ± 0.24	This work
V (km s ⁻¹)	-73.37 ± 0.36	This work
W (km s ⁻¹)	39.45 ± 0.33	This work
<i>S_{tot}</i> (km s ⁻¹)	85.73 ± 0.35	This work

^a: Correction of -17μ s applied to the Gaia parallax following the prescription in Lindegren et al. (2020)

2.2. Astrometry & Photometry

Stellar astrometry and visible and infrared photometry are compiled in Table 1. The positions, proper motions, parallax, and *Gaia* photometry are from Gaia EDR3 (van Leeuwen et al. 2021), while the radial velocity is from GaiaDR2 (Gaia Collaboration et al. 2018).

¹ <https://tev.mit.edu/data/collection/193/>

We convert the astrometry to Galactic velocities following (ESA 1997)². Photometry is reported from APASS Data Release 10 (Henden et al. 2016)³, the TESS Input Catalog (TIC8), 2MASS (Cutri et al. 2003), and WISE (Cutri et al. 2012).

2.3. Spectral Energy Distribution

We analyzed TOI-1231’s broadband spectral energy distribution (SED) alongside its *Gaia* EDR3 parallax to determine an empirical measurement of the star’s radius, following Stassun & Torres (2016); Stassun et al. (2017, 2018). Together, the available photometry described here and listed in Table 1 cover the full stellar SED from 0.4–22 μm (see Figure 1). We exclude the APASS/DR10 data from the SED fit in favor of the *Gaia* EDR3 passbands, which cover the same wavelength range and have smaller errors, but note that we adopt an error floor of 0.03 mag on the photometry because the systematics on the absolute flux calibration between photometric systems is 2–3%.

We performed the fit using NextGen stellar atmosphere models, placing a prior on the star’s surface gravity ($\log g$) from the TESS Input Catalog (TIC-8). We set the stellar effective temperature equal to the result from the Cool Dwarf Catalog ($T_{\text{eff}} = 3557 \pm 82$ K, Muirhead et al. 2018) and the extinction to zero due to the star’s proximity (within the Local Bubble) which is consistent with the reddening value of $E_{B-V} = 0.001 \pm 0.015$ from Lallement et al. (2018)⁴. The resulting SED fit is quite good (Figure 1, top) with a reduced χ^2 of 1.9. The best fit stellar metallicity is $[\text{Fe}/\text{H}] = 0.0 \pm 0.3$. Integrating the model SED results in the bolometric flux at Earth being $F_{\text{bol}} = (1.345 \pm 0.047) \times 10^{-9}$ erg s⁻¹ cm⁻² ($m_{\text{bol}} = 10.682 \pm 0.032$ on IAU 2015 bolometric magnitude scale)⁵. Taking the F_{bol} and T_{eff} together with the *Gaia* EDR3 parallax gives the stellar radius as $R_{\star} = 0.466 \pm 0.021 R_{\odot}$ and the stellar mass as $M_{\star} = 0.485 \pm$

0.024 M_{\odot} based on the empirical M_{K_s} vs. mass relations from Mann et al. (2019)⁶.

2.3.1. Speckle Observations

High-angular resolution imaging is needed to search for nearby sources that can contaminate the TESS photometry, resulting in a diluted transit and an underestimated planetary radius, and also to search for faint stars that might be responsible for the transit signal. We searched for nearby sources to TOI-1231 with SOAR speckle imaging (Tokovinin et al. 2018) on UT 12 December 2019 in I-band, a similar near-IR bandpass as used by *TESS*. Further details of observations from the SOAR *TESS* survey are available in Ziegler et al. (2020). We detected no nearby stars within 3'' of TOI-1231 within the 5σ detection sensitivity limits of the observation, which are plotted along with the speckle auto-correlation function in the middle panel of Figure 1. Using the measured detection sensitivity from the SOAR observation and the estimated T_{eff} of the target star along with main-sequence stellar SEDs (Kraus & Hillenbrand 2012), we can effectively rule out a main-sequence companion within angular resolutions between 0.2'' to 3.0'' or projected physical separations of 5.5 au to 83 au.

Speckle interferometric images of TOI-1231 were also obtained on UT 13 March 2020 using the Zorro⁷ instrument mounted on Gemini-South. Zorro observes simultaneously in two bands (832 \pm 40 nm and 562 \pm 54 nm) obtaining diffraction limited images with inner working angles of 0.026 and 0.017 arcseconds, respectively. The TOI-1231 data set consisted of 5 minutes of total integration time taken as sets of 1000 \times 0.06 sec images. All the images were combined using Fourier analysis techniques, examined for stellar companions, and used to produce reconstructed speckle images (see Howell et al. 2011). The speckle imaging results reveal TOI-1231 to be a single star to contrast limits of ~ 5 to 8 magnitudes, eliminating the possibility of any main sequence companions to TOI-1231 ($d = 27.6$ pc) within the spatial limits of 3 to 33 au (Figure 1, bottom).

2.4. Stellar Kinematics and Population

Using the astrometry and radial velocity data from *Gaia* Collaboration et al. (2018), we calculate the heliocentric Galactic velocity for TOI-1231 to be $(U, V, W) = (-20.25, -73.37, 39.45 \pm 0.24, 0.36, 0.33)$ km s⁻¹, with total velocity $S_{\text{tot}} = 85.73 \pm 0.35$ km s⁻¹. Compared to the Local Standard of Rest (LSR) of Schönrich et al.

² U towards Galactic center, V in direction of Galactic spin, and W towards North Galactic Pole (ESA 1997).

³ <https://www.aavso.org/apass>

⁴ STILISM: <https://stilism.obspm.fr/>

⁵ Besides this analysis, we also estimate m_{bol} via other methods. Applying the M dwarf bolometric magnitude relations of Casagrande et al. (2008) with the 2MASS JHK_s photometry, we estimate $m_{\text{bol}} = 10.74 \pm 0.02$. Using the $V - J$ vs. BC_{K_s} relation from Mann et al. (2015) applied to the 2MASS K_s magnitude we estimate $m_{\text{bol}} = 10.79$. Fitting BT-Settl-CIFIST synthetic spectra to the photometry in Table 1 using the VOSA SED Analyzer (Bayo et al. 2008) yielded $F_{\text{bol}} = (1.363 \pm 0.116) \times 10^{-9}$ erg s⁻¹ cm⁻² ($m_{\text{bol}} = 10.666 \pm 0.095$) for $T_{\text{eff}} = 3600$ K, $\log g = 4.5$, $[\text{M}/\text{H}] = 0$. These values provide independent checks, but we adopt the F_{bol} and m_{bol} in the text.

⁶ For $M_{K_s} = 5.861 \pm 0.026$ and assuming $[\text{Fe}/\text{H}] = 0$.

⁷ <https://www.gemini.edu/sciops/instruments/alopeke-zorro/>

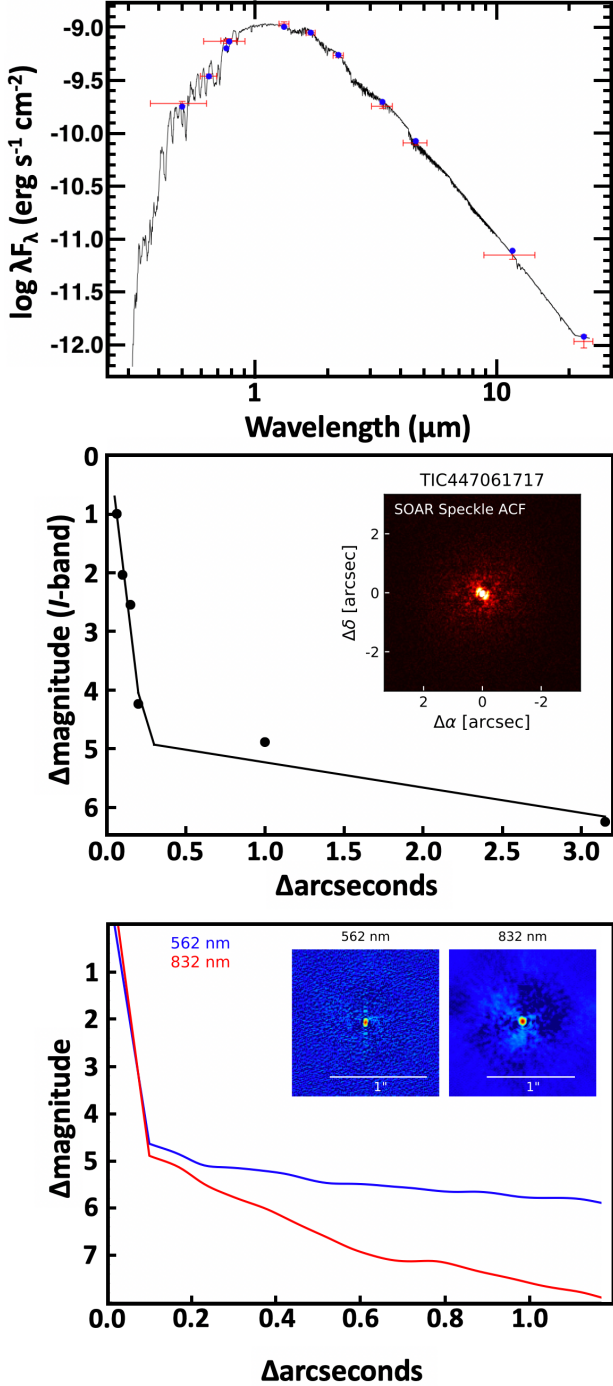


Figure 1. *Top:* Best fit SED for TOI-1231. The red symbols are the observed photometric measurements and the horizontal lines show the effective width of each filter. The blue symbols depict the model flux values from the best-fit NextGen atmosphere model, which is shown in black. *Middle:* SOAR contrast curve and image (inset) for I-band speckle observations of TOI-1231. *Bottom:* Zorro contrast curves and images (inset) for 562 nm and 832 nm speckle observations of TOI-1231. No visual companions are detected in the field of view of either SOAR or Zorro.

(2010), we estimate velocities of $(U, V, W) = (-10.2, -62.4, 46.5)$ km s⁻¹, with $S_{LSR} = 78.4$ km s⁻¹. We use the BANYAN Σ (Bayesian Analysis for Nearby Young AssociatioNs Σ ; Gagné et al. 2018) tool to estimate membership probabilities to nearby young associations within 150 pc, however the probabilities are $\ll 0.1\%$ for any of the known nearby stellar groups (all with ages < 1 Gyr), and the star is classified as “field”. Following Bensby et al. (2014), we use the Galactic velocity to estimate kinematic membership probabilities to the Milky Way’s principal populations, using a 4-population model for the thin disk, thick disk, halo, and the Hercules stream⁸. We estimate kinematic membership probabilities of $P(\text{thin}) = 16.7\%$, $P(\text{thick}) = 64.5\%$, $P(\text{Hercules}) = 18.7\%$, and $P(\text{halo}) = 0.06\%$. However, the star’s LSR velocity places it among the Hercules stream member in Fig. 29 of Bensby et al. (2014). Mackereth & Bovy (2018) calculated parameters of the star’s Galactic orbit using Stäckel approximation with the Gaia Collaboration et al. (2018) astrometry, and find an eccentricity of 0.332, $z_{max} = 0.905$ kpc, perigalacticon of $r_{peri} = 4.02$ kpc and apogalacticon of $r_{ap} = 8.03$ kpc⁹, i.e. we are catching the star near its apogalacticon.

We also searched for companions of TOI-1231 in the Gaia Collaboration et al. (2018) catalog via the 50 pc sample of Torres et al. (2019). Given the mass of $0.46 M_\odot$, we estimate the tidal radius for TOI-1231 (where bound companions would likely be found) to be 1.04 pc (Mamajek et al. 2013), which corresponds to a projected radius of $\sim 2^\circ$. Querying the Torres et al. (2019) catalog for stars with proper motions and parallaxes within 20% of that of the star within 2 tidal radii ($4^\circ.4$) yielded no candidate companion. Therefore, we conclude TOI-1231 to be a single star.

2.5. Metallicity

The $V - K_s$ vs. absolute magnitude position of an M dwarf can be used to infer a photometric metallicity estimate (e.g. Johnson & Apps 2009). TOI-1231’s combination of $V - K_s$ color (4.25) and absolute magnitude ($M_{K_s} = 5.86$) are consistent with it being 0.17 mag brighter than the locus for nearby M dwarfs, which Schlaufman & Laughlin (2010) estimate represents an isometallicity trend of $[\text{Fe}/\text{H}] = -0.14$. Using the calibrations of Johnson & Apps (2009) and Schlaufman &

⁸ The Hercules stream stars contain a mix of α -enhanced old stars and younger less α -enhanced around the solar $[\text{Fe}/\text{H}]$ (e.g. Bensby et al. 2014), likely from the inner part of the Galaxy and kinematically heated by the Galactic bar (Dehnen 2000) and halo, although the exact type of resonant interaction responsible for the stream is still controversial (Monari et al. 2019).

⁹ $R_O = 8$ kpc is assumed.

Laughlin (2010), this offset is consistent with a predicted metallicity of $[\text{Fe}/\text{H}] = +0.05$ and -0.03 , respectively, i.e., approximately solar.

Gaia DR2 (Gaia Collaboration et al. 2018) has an estimate of $[\text{Fe}/\text{H}] = -1.5$, but for an unrealistic giant-like surface gravity of $\log g = 3.0$ and hot T_{eff} of 4000 K. Taken at face value, the Gaia DR2 metallicity would predict that the star’s $V - K_s$ vs. M_{K_s} position should be more than a magnitude below the main sequence (extrapolating the metallicity vs. ΔM_{K_s} relations of Schlafman & Laughlin 2010), well below where it is observed (~ 0.2 mag above the MS).

Anders et al. (2019) uses the *StarHorse* code to fit G_B , G , G_R , J , H , K_s , $W1$, and $W2$ photometry to solve for a photometric metallicity estimate consistent with $[\text{Fe}/\text{H}] = 0.095^{+0.028}_{-0.061}$.

Taking the mean of our independent photometric metallicity estimates and that of Anders et al. (2019), we adopt a metallicity of $[\text{Fe}/\text{H}] = +0.05 \pm 0.08$.

3. EXOPLANET DETECTION & FOLLOW UP

3.1. TESS Time Series Photometry

TOI-1231 was selected for transit detection observations by *TESS* from two input lists. It was included in the exoplanet candidate target list (CTL) that accompanied version 8 of the TESS Input Catalog (TIC; Stassun et al. 2019), and also in the Cool Dwarf Catalog (Muirhead et al. 2018). Its CTL observing priority was 0.00734, placing it among the top 3% of targets selected for transit detection by the mission, due to its brightness and small estimated stellar radius (see sections 3.1 and 3.3 of Stassun et al. (2019) for details on the prioritization process). It was also selected for observations by TESS Guest Investigator proposal GO11180 (C. Dressing). TOI-1231 was observed by *TESS* from UT 28 February through 26 March 2019 as part of the Sector 9 campaign and again from UT 26 March through 22 April 2019 as part of Sector 10. The star fell on Camera 3 in both sectors, but shifted from CCD 1 in Sector 9 to CCD 2 in Sector 10.

The SPOC data for TOI-1231 can be accessed at the the Mikulski Archive for Space Telescopes (MAST) website¹⁰, and includes both the simple aperture photometry (SAP) flux measurements (Twicken et al. 2010; Morris et al. 2017) and the presearch data conditioned simple aperture photometry (PDCSAP) flux measurements (Smith et al. 2012; Stumpe et al. 2012, 2014). These data products differ in that the instrumental variations present in the SAP measurements are removed from the

PDCSAP data. The main variations are due to thermal effects and strong scattered light present at the start of each orbit, which impact the systematic error removal in PDC (see *TESS* data release notes¹¹ DRN16 and DRN17). We therefore use the quality flags provided by SPOC to mask out unreliable segments of the time series before executing the global fitting process in Section 4. We further detrend the *TESS* data by separating the individual spacecraft orbits (two in each sector) and fitting each orbit’s flux measurements with a low order spline in order to mitigate residual trends in the photometry (Figure 2).

3.1.1. TESS Transit Detection

TOI-1231 b transited once in each of sectors 9 and 10. It was first identified as a planet candidate five months prior to becoming a TOI, by the TESS Single Transit Planet Candidate Working Group (TSTPC WG). The TSTPC WG focuses on searching light curves produced by the MIT Quick Look Pipeline for single transit events, and validating and/or confirming those that are true planets, with the aim of increasing the yield of intermediate-to-long-period planets found by *TESS* (Villanueva et al. 2019, Villanueva et al. in prep.).

The two transits of TOI-1231 b were later also detected by both the MIT Quick Look Pipeline (QLP), which searches for evidence of planet candidates in the *TESS* 30 minute cadence Full Frame Images, and the SPOC pipeline, which analyzes the 2-minute cadence data that *TESS* obtains for pre-selected target stars (Jenkins et al. 2016b). The *TESS* transits, one of which occurs in Sector 9 and the other in Sector 10, have a measured depth of 6453 ppm, a duration of 3.26 hours, and a measured period of 24.246 days.

While the depth and flat bottomed shape of the TOI-1231 transits were suggestive of the transit signal being planetary in nature, there are a variety of false positives that can mimic this combination. The main source of false positives in the TESS Objects of Interest (TOIs) are eclipsing binaries, either as two transiting stars on grazing orbits or in the case of a background blend which reduces the amplitude of a foreground eclipsing binary signal, causing it to be fallaciously small (e.g. Cameron 2012). The *TESS* vetting process is designed to guard against these false positives, and so we inspected the star’s Data Validation Report (DVR, Twicken et al. 2018; Li et al. 2019), which is based upon the SPOC two minute cadence data. The multi-sector DVR shows no signs of secondary eclipses, odd/even transit depth inconsistencies, nor correlations between the depth of the

¹⁰ <https://mast.stsci.edu>

¹¹ https://archive.stsci.edu/tess/tess_drn.html

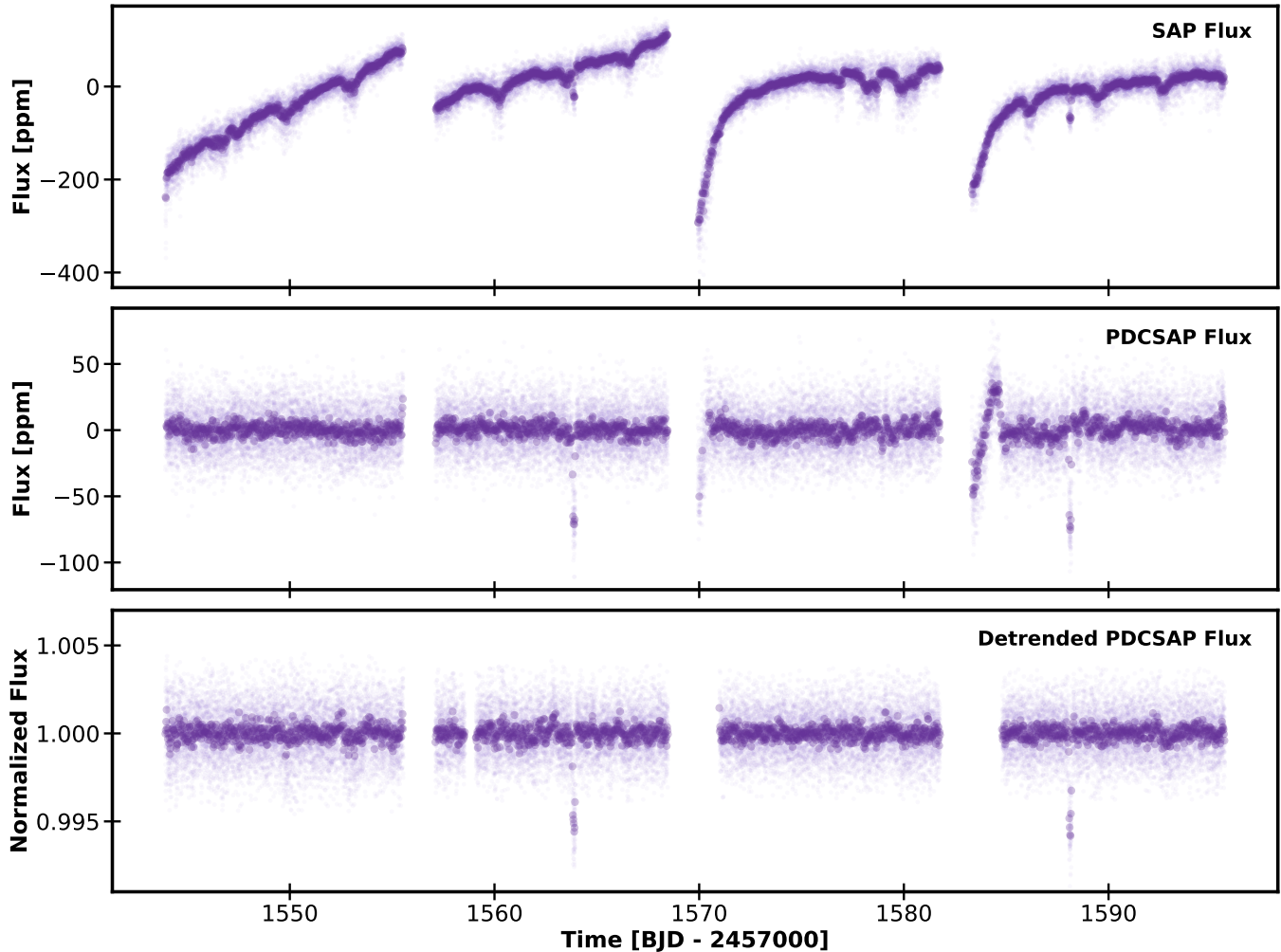


Figure 2. TESS light curves: Simple Aperture Photometry (*SAP*, *top*), presearch data conditioned SAP (*PDCSAP*, *middle*), and orbit-by-orbit detrended PDCSAP (*bottom*). Lighter points depict the *TESS* two-minute cadence flux measurements, darker points are the same data binned into 30 minute intervals. The two transit events can be clearly seen as brief flux dips in the middle and bottom panels.

transit and the size of the aperture used to extract the light curve, any of which would indicate that the transit signal originated from by a nearby eclipsing binary. The DVR also showed that the location of the transit source is consistent with the position of the target star. Upon passing these vetting checks, the transit signal was assigned the identifier TOI-1231.01 and announced on the MIT *TESS* data alerts website¹² (Guerrero et al. 2021).

3.2. Ground-based Time-Series Photometry

We acquired ground-based time-series follow-up photometry of TOI-1231 during the times of transit predicted by the *TESS* data. We used the *TESS* Transit

Finder, which is a customized version of the *Tapir* software package (Jensen 2013), to schedule our transit observations.

3.2.1. LCO 1m Observations

Two partial transits of TOI-1231 b were observed using the Las Cumbres Observatory Global Telescope (LCOGT) 1m network (Brown et al. 2013) in the PANSTARSS *z* band on UTC 2020 January 16 by the LCOGT node at Cerro Tololo Inter-American Observatory and May 6 2020 by the LCOGT node at Siding Spring Observatory (Figure 5, second panel). The telescopes are equipped with 4096×4096 LCO SINISTRO cameras having an image scale of $0''.389 \text{ pixel}^{-1}$ resulting in a $26' \times 26'$ field of view. The images were calibrated by the standard LCOGT BANZAI pipeline and the photo-

¹² <http://tess.mit.edu/alerts>

metric data were extracted using the `AstroImageJ` (AIJ) software package (Collins et al. 2017). Circular apertures with radius 12 pixels ($4''.7$) were used to extract the differential photometry.

3.2.2. ASTEP 0.4m Observations

We observed two full transits of TOI-1231 with the Antarctica Search for Transiting ExoPlanets (ASTEP) program on the East Antarctic plateau (Guillot et al. 2015; Mékarnia et al. 2016). The 0.4m telescope is equipped with an FLI Proline science camera with a KAF-16801E, 4096×4096 front-illuminated CCD. The camera has an image scale of $0''.93 \text{ pixel}^{-1}$ resulting in a $1^\circ \times 1^\circ$ corrected field of view. The focal instrument dichroic plate splits the beam into a blue wavelength channel for guiding, and a non-filtered red science channel roughly matching an R_c transmission curve. The telescope is automated or remotely operated when needed. Due to the extremely low data transmission rate at the Concordia Station, the data are processed on-site using an automated IDL-based pipeline, and the result is reported via email and then transferred to Europe on a server in Roma, Italy. The raw light curves of about 1,000 stars are then available for deeper analysis. These data files contain each star’s flux computed through various fixed circular apertures radii, so that optimal lightcurves can be extracted (Figure 5, third panel). For TOI-1231 an 11 pixels ($10''.3$) radius aperture was found to give the best results.

The observations took place on UTC 2020 May 6 and August 11. Weather was good to acceptable, and air temperatures ranged between -50°C and -70°C . Two full transits, including the ingress and egress, were detected. Two other transits of TOI-1231 b were also detected on May 30 and June 26, but were partial or affected by technical issues, are generally of lower signal-to-noise and are thus not included in the present analysis. In each case, the ingress and egress occurred at the predicted times (with an uncertainty of a few minutes or less), indicating that any transit time variation must be small.

3.2.3. ExTrA 0.6m Observations

The ExTrA facility (Bonfils et al. 2015), located at La Silla observatory, consists of a near-infrared (0.85 to $1.55 \mu\text{m}$) multi-object spectrograph fed by three 60-cm telescopes. At the focal plane of each telescope five fiber positioners pick the light from the target and four comparison stars. We observed two full transits of TOI-1231 b on UTC 2020 March 18 and 2021 January 27 (Figure 3). The first night we observed with three telescopes using the fibers with $8''$ apertures. The second night we observed with two telescopes and $4''$ aperture

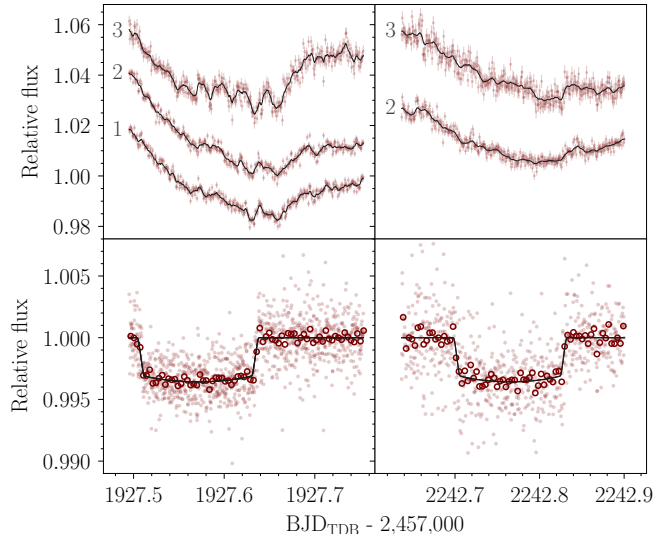


Figure 3. Light curves obtained by the ExTrA facility on nights UTC 2020 March 18 (left) and 2021 January 27 (right). Top panels show the Raw ExTrA photometry of each telescope (labeled 1, 2, and 3), displaced vertically for clarity and a black curve depicting the median of the posterior of the modeling. Bottom panels show the light curves after correction with the maximum a posteriori model, with individual observations as light points, 5 minute bins as dark circles, and the maximum a posteriori transit model as a black line.

fibers. Both nights we used the high resolution mode of the spectrograph ($R \sim 200$) and 60-seconds exposures. We also observed 2MASS J10283882-5234151, 2MASS J10285562-5220140, 2MASS J10273532-5206553, and 2MASS J10271569-5239330, with J-magnitude (Skrutskie et al. 2006) and T_{eff} (Gaia Collaboration et al. 2018) similar to TOI-1231, for use as comparison stars. The resulting ExTrA data were analysed using custom data reduction software.

The ExTrA light curves are affected by systematic effects that are currently under investigation. To account for them, we modeled the transits observed by ExTrA with `juliet` (Espinoza et al. 2019; Kreidberg 2015; Speagle 2020), and included the quasi-periodic kernel Gaussian Process implemented in `celerite` (Foreman-Mackey et al. 2017), with different kernel hyperparameters for each ExTrA telescope and for each night. We used a prior for the stellar density of $\rho_* = 6.48 \pm 0.30 \text{ g cm}^{-3}$ (Stassun et al. 2019), and non-informative priors for the rest of the parameters. The posterior provides the timings of the observed transits: $2458927.5716 \pm 0.0013 \text{ BJD}_{\text{TDB}}$, and $2459242.7657 \pm 0.0013 \text{ BJD}_{\text{TDB}}$, a planet to star radius ratio of $R_P/R_* = 0.0660^{+0.0072}_{-0.0086}$, and an impact parameter of $b = 0.201^{+0.091}_{-0.12}$. These transit light curves are not

used in the global EXOFASTv2 fit described in Section 4 in order to avoid biasing the final results due to the systematics present in the ExTrA data. However, the timing of the second transit is used as a prior for the time of conjunction (T_C) to better constrain the period of the planet.

3.3. Time Series Radial Velocities

Shortly after the discovery of the planet candidate by the TSTPC WG, we began radial velocity (RV) follow up efforts using the Planet Finder Spectrograph (PFS) on Las Campanas Observatory’s 6.5m Magellan Clay telescope (Crane et al. 2006, 2008, 2010). PFS is an iodine cell-based precision RV spectrograph with an average resolution of $R \simeq 130,000$. RV values are measured by placing a cell of gaseous I_2 , which has been scanned at a resolution of 1 million using the NIST FTS spectrometer (Nave 2017), in the converging beam of the telescope. This cell imprints the 5000-6200Å region of the incoming stellar spectra with a dense forest of I_2 lines that act as a wavelength calibrator and provide a proxy for the point spread function (PSF) of the spectrometer (Marcy & Butler 1992).

The spectra are split into 2Å chunks, each of which is analyzed using the spectral synthesis technique described in Butler et al. (1996), which deconvolves the stellar spectrum from the I_2 absorption lines and produces an independent measure of the wavelength, instrument PSF, and Doppler shift. The final Doppler velocity from a given observation is the weighted mean of the velocities of all the individual chunks (~ 800 for PFS). The final internal uncertainty of each velocity is the standard deviation of all 800 chunk velocities about that mean.

A total of 28 PFS radial observations were obtained from May 2019 to February 2020, binned into 14 velocity measurements, with a mean internal uncertainty of 1.22 m s^{-1} (Table 2). A Generalized Lomb-Scargle (GLS) periodogram of the PFS RV data shows a significant peak at 24 days (Figure 4), which matches the orbital period determined from the *TESS* data.

4. SYSTEM PARAMETERS FROM EXOFASTV2

To fully characterize the TOI-1231 system, we used the EXOFASTv2 software package (Eastman et al. 2013, 2019) to perform a simultaneous fit to the star’s broadband photometry, the *TESS*, LCO, and ASTEP time series photometry, and the PFS radial velocity measurements. We applied Gaussian priors to the parallax and V-band extinction of the star using the results of Gaia EDR3 ($\varpi = 36.3726 \pm 0.0163$, corrected using the Lindgren et al. (2020) prescription) and Lallement et al.

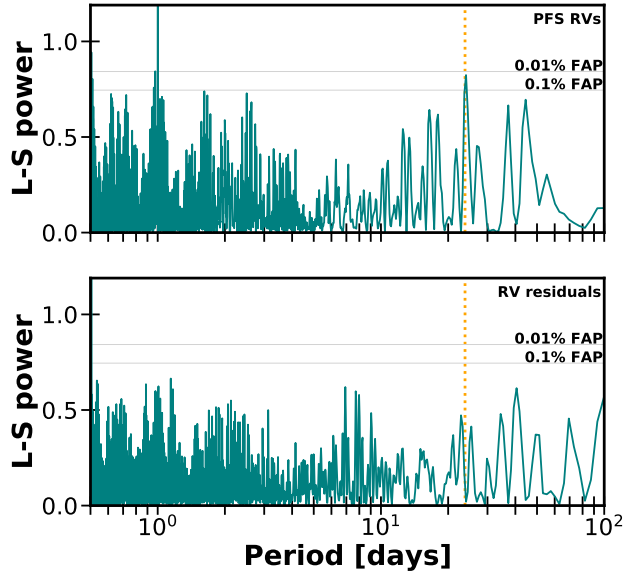


Figure 4. *Top:* Generalized Lomb-Scargle periodogram of the radial velocity measurements from PFS. There is a clear peak at period of TOI-1231 b (orange dotted line). *Bottom:* GLS of the radial velocity residuals, after the signal for planet b has been removed. No significant peaks remain in the data to suggest the presence of additional planets and/or stellar rotational signals.

Table 2. Binned RV data of TOI-1231

Date [BJD _{TDB}]	RV [m s^{-1}]	σ_{RV} [m s^{-1}]
2458618.501473	-10.13	1.19
2458625.551234	0.32	1.44
2458627.574495	3.73	1.17
2458677.491563	7.16	1.27
2458679.483330	5.96	1.22
2458685.500395	2.12	1.44
2458827.826089	3.29	1.06
2458828.842260	-0.34	1.08
2458833.804469	-9.11	1.27
2458836.814827	-4.43	1.01
2458883.799738	-4.85	1.21
2458885.807135	-0.57	1.24
2458886.798816	-2.90	1.31
2458890.781648	1.10	1.17

(2018) ($A_v = 0.003 \pm 0.0465$), respectively. Gaussian priors were also placed on the TOI-1231’s mass ($M_\star = 0.461 \pm 0.018 M_\odot$, calculated using the prescription in Mann et al. 2019), effective temperature ($T_{\text{eff}} = 3562 \pm 101 \text{ K}$, taken from Gaidos et al. 2014) and metallicity ($[\text{Fe}/\text{H}] = 0.05 \pm 0.08$ (see S2.5 for details). We disabled EXOFASTv2’s MIST isochrone fitting option, which is less

reliable for low mass stars (Eastman et al. 2019). Finally, we placed a prior on the planet’s time of conjunction derived from the ExTrA photometry (3.2.3). We did not place any constraints on the planet’s period or orbital eccentricity.

EXOFASTv2’s SED fitting methodology differs from the approach used in the SED-only fit that helped verify TOI-1231’s suitability for PRV follow up in Section 2.3. In place of the NextGen atmospheric models, EXOFASTv2 instead uses pre-computed bolometric corrections in a grid of $\log g$, T_{eff} , $[\text{Fe}/\text{H}]$, and V-band extinction¹³. This grid is based on the ATLAS/SYNTHÉ stellar atmospheres (Kurucz 2005) and the detailed shapes of the broadband photometric filters.

We note that neither the raw TESS time series photometry nor the PFS RV measurements exhibit the type of sinusoidal variations that we would expect to see if the star was subject to rotation-based activity due to active regions such as star spots or plages crossing the visible hemisphere (Saar & Donahue 1997; Robertson et al. 2020). This lack of rotational modulation suggests an inactive star, a claim further supported by the lack of emission or any detectable temporal changes in the core of the H- α line (see, e.g., Reiners et al. 2012; Robertson et al. 2013). We therefore do not include any additional activity-based terms or detrending efforts when fitting either the photometric or radial velocity data.

The median EXOFASTv2 parameters for the TOI-1231 system are shown in Table 3 and the best fits to the TESS, LCO, and ASTEP photometry and the PFS radial velocity data are shown in Figure 5. The scatter in a star’s radial velocity measurements includes any unmodeled instrumental effects or stellar variability. To address this, we include a ‘jitter’ term in the RV fit which is used to encompass uncorrelated signals in the star’s own variability or PFS’s systematics that occur on timescales shorter than the observational baseline. This value is added in quadrature to the internal uncertainties reported in the PFS data set to produce the RV error bars seen in Figure 5. The best fit orbital eccentricity ($e = 0.087^{+0.012}_{-0.061}$) should not be regarded as statistically significant as it does not meet the criteria of being at least 2.45σ from 0 that is necessary to avoid falling subject to the Lucy-Sweeney bias (Lucy & Sweeney 1971). Even though the best fit eccentricity is consistent with a circular orbit, we do not enforce a zero eccentricity fit because even a small amount of non-modeled eccentricity can bias the resulting orbital parameters and underestimate the uncertainties in many covariant parameters.

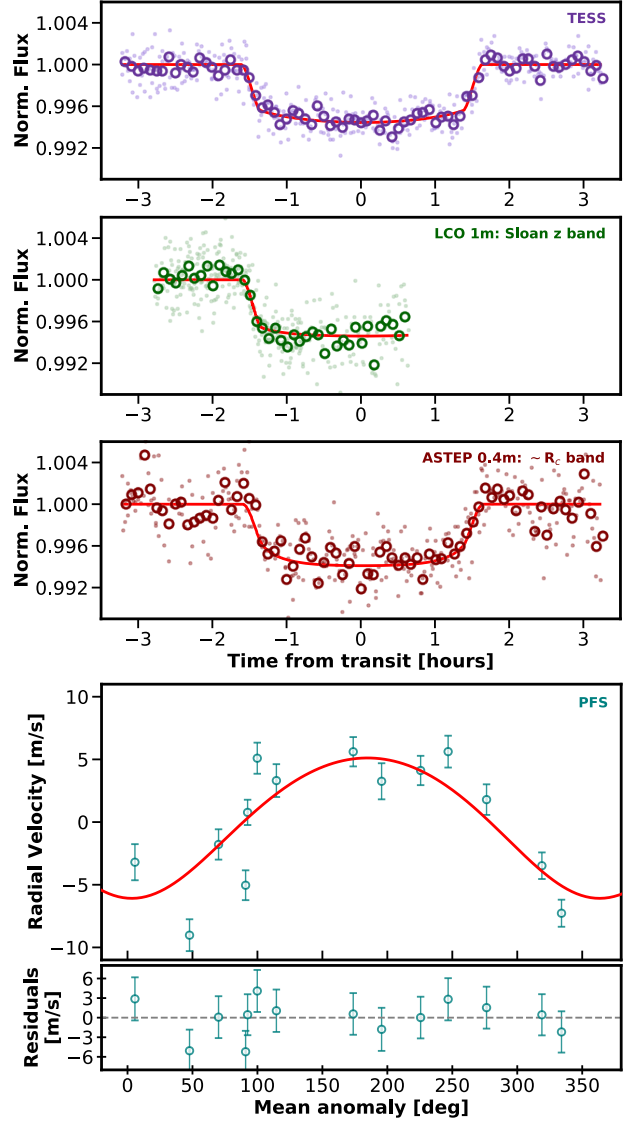


Figure 5. Results of the EXOFASTv2 joint fit to the TESS photometry, ground-based LCO and ASTEP, and the PFS radial velocities. The top three panels show the phase folded photometry data from TESS (two full transits), LCO (two partial transits), and ASTEP (two full transits). All three photometry panels depict the unbinned data as light points, the five minute binned data as dark circles, and the best fit model as a solid red line. The bottom panel shows the phase folded RV measurements from PFS in cyan and the best fit model in red. The RV residuals after the best fit model has been subtracted from the data are displayed underneath the fit. Error bars in both RV panels are the quadrature sum of the PFS internal uncertainties and the RV jitter estimate from the EXOFASTv2 fit.

The mass of TOI-1231 b is measured to be $15.5 \pm 3.3 M_{\oplus}$, which, when combined with the measured planet radius of $3.65^{+0.16}_{-0.15} R_{\oplus}$, results in a bulk density of

¹³ http://waps.cfa.harvard.edu/MIST/model_grids.html#bolometric

$1.74_{-0.42}^{+0.47} \text{ g cm}^{-3}$ making the planet slightly denser than Neptune ($\rho_{Nept} = 1.638 \text{ g cm}^{-3}$).

5. DISCUSSION

Barclay et al. (2018) predict that *TESS* will find just one non-rocky Neptune-sized or smaller planet in the habitable zone of a M dwarf brighter than $J = 10$. While the final number may be slightly higher, TOI-1231 b is the first confirmed *TESS* planet to meet these criteria. One method for comparing planets’ potential for atmospheric characterization via transmission spectroscopy is the Transmission Spectroscopy Metric (TSM, Kempton et al. 2018). A planet’s TSM is proportional to its transmission spectroscopy signal-to-noise and is based on the strength of its expected spectral features (derived from its radius and scale height and the radius of the host star) and the host star’s apparent J-band magnitude. With a transmission spectroscopy metric (TSM) of 99 ± 25 , TOI-1231 b planet ranks among the highest TSM Neptunes of any temperature in the pre-*TESS* era (Figure 6, Guo et al. 2020).

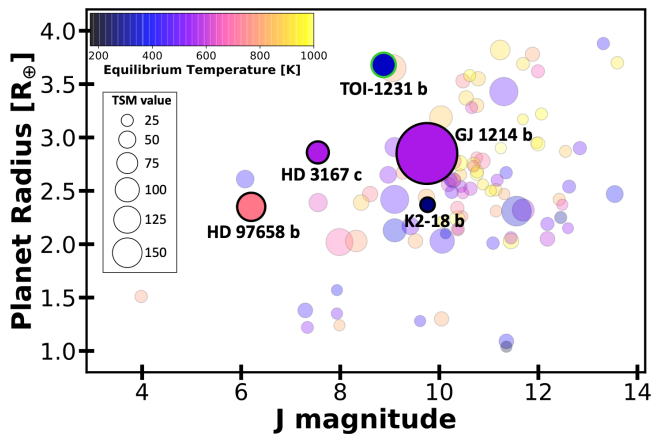


Figure 6. Transmission spectroscopy metric (TSM) values for small planets with $T_{eq} < 1000\text{K}$ compared to their radii and host star’s J magnitude, data are taken from Guo et al. (2020). The four planets that have already had their atmospheres characterized by HST are shown as solid circles and labeled. TOI-1231 b (green outline) offers another promising target in the cool, small planet regime and would, for the first time, enable comparisons in the $T_{eq} = 250\text{-}350 \text{ K}$ range when contrasted with K2-18 b.

TOI-1231 b is one of the coolest planets accessible for atmospheric studies with $T_{eq} = 330 \text{ K}$ ¹⁴. Until recently it appeared that cooler planets had smaller spectral fea-

¹⁴ We note that T_{eq} is calculated using Eqn. 1 of Hansen & Barman (2007), which assumes no albedo and perfect redistribution. As such the quoted statistical error is likely severely underestimated relative to the systemic errors inherent in this assumption.

tures, perhaps due to the increasing number of condensates that can form at lower temperatures (Crossfield & Kreidberg 2017). However, new observations of water features in the habitable-zone planet K2-18 b break this trend (Tsiaras et al. 2019; Benneke et al. 2019b). The K2-18 b water feature is very intriguing: it is suggestive of a qualitative change in atmospheric properties near the habitable zone. Perhaps condensates rain out (analogous to the L/T transition in brown dwarfs), and/or photochemical haze production is less efficient (Saumon & Marley 2008; Morley et al. 2013). However, K2-18 b is the only planet below 350 K with a measured transmission spectrum. TOI-1231 b provides an intriguing addition to the atmospheric characterization sample in this temperature range to determine whether K2-18 b is representative or an outlier. Recently, four HST transit observations were awarded to measure the near-infrared transmission spectrum of TOI-1231 b with the Wide Field Camera 3 (WFC3) instrument (GO 16181; PI L. Kreidberg).

5.1. Simulated Atmospheric Retrievals

In order to estimate how well the atmospheric properties could be extracted with HST, we used the open-source *petitRADTRANS* package (Mollière et al. 2019) to derive transmission spectra of TOI-1231 b, based on a simple atmospheric model. The atmosphere probed by the observations was assumed to be isothermal, at the equilibrium temperature derived for the planet in this work. Next, equilibrium chemistry was used to calculate the absorber abundances in the atmosphere, obtained with the chemistry model that is part of *petitCODE* (Mollière et al. 2017). We assumed two different compositional setups, 3 and $100 \times$ solar (Jupiter and Neptune-like, respectively), at a solar C/O. In addition, we introduced a gray cloud deck and modeled its effect on the spectrum when placing it between 100 and 10^{-6} bar, in 1 dex steps. The model with the highest cloud pressure was assumed to be our cloud-free model, because the atmosphere will become optically thick at lower pressures. We included the gas opacities of the following line absorbers: H_2O , CH_4 , CO , CO_2 , Na, and K. In addition to the gray cloud, continuum opacity sources arising from H_2 , He, CO , H_2O , CH_4 , and CO_2 Rayleigh scattering, as well as $\text{H}_2\text{-H}_2$ and $\text{H}_2\text{-He}$ collision-induced absorption, were included. We refer the reader to Mollière et al. (2019) for the references used for the opacities.

We generated mock observations for all cases described above and retrieved them with *petitRADTRANS*, using the *PyMultiNest* package (Buchner et al. 2014). The latter uses the nested sampling implementation *MultiNest* (Feroz et al. 2009). The synthetic HST

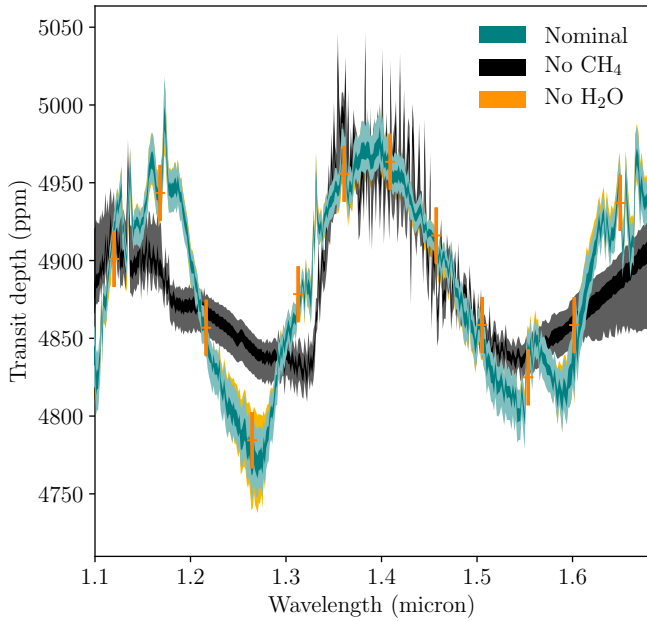


Figure 7. Synthetic HST observations and retrieval of the clear, $100 \times$ solar enrichment case. The 16-18 and 2-98 percentile envelopes of the retrieved flux distribution are shown for the retrievals with the full model (green envelopes) and the model neglecting CH_4 or H_2O (black or orange envelopes, respectively).

WCF3 observations were created assuming a wavelength range of 1.12 to 1.65 μm , with 12 points spaced equidistantly in wavelength space. We estimated the uncertainties on the spectroscopic transit depths using the `Pandexo_HST` tool¹⁵. Assuming four HST transit observations, we expect uncertainties of 18 ppm on the transit in each spectral channel. This corresponds to ~ 0.6 times the transit signal of the planet’s scale height, when assuming a $100 \times$ solar composition. For these retrievals we placed special emphasis on the detectability of H_2O and CH_4 , for which we implemented the method described in [Benneke & Seager \(2013\)](#): the abundances of all metal absorbers were retrieved freely, assuming vertically constant abundance profiles. The abundance of H_2 and He was found by requiring that the mass fractions of all species (metals + H_2 and He) add up to unity, with an abundance ratio of 3:1 between H_2 and He. Three retrievals were run for every synthetic observation. (i): nominal model, retrieving the abundances of all metal absorbers, as well as the cloud deck pressure. (ii): same as (i), but neglecting the CH_4 opacity and CH_4 abundance as a free parameter. (iii): same as (i), but neglecting the H_2O opacity and H_2O abundance as a free parameter.

¹⁵ <https://exoctk.stsci.edu/>

For every synthetic observation we then derived three evidences for models (i), (ii), and (iii), using nested sampling retrievals. The Bayes factor B , which is the ratio of these evidences, then allows us to assess how strongly models including CH_4 or H_2O are preferred (Bayes factor of models (i) and (ii) or models (i) and (iii), respectively). We used a boundary value of $B > 3$ to express strong preference for a given model, following [Kass & Raftery \(1995\)](#).

We show the synthetic HST observation of the clear, $100 \times$ solar case in Figure 7. Because the $100 \times$ solar case has a larger mean molecular weight, it is the more challenging of the two enrichment cases. In addition to the synthetic observation, the 16-18 and 2-98 percentile envelopes of the retrieved transit depth distribution are shown for the retrievals with models (i), (ii), and (iii), that is the full model and the model neglecting the CH_4 or H_2O opacity, respectively.

For these cases, we find very strong preference for including CH_4 in the model ($B = 10^8$) and no preference for including H_2O (H_2O and CH_4 have roughly equal abundances in the input model but the CH_4 opacity is larger than the H_2O opacity at all wavelengths). Clouds are a possibility for such planets ([Crossfield & Kreidberg 2017](#)) and we find that from $P_{\text{cloud}} < 1$ mbar on it becomes challenging to detect atmospheric features at all, and the three models (i), (ii) and (iii) become indistinguishable. In summary, we conclude that TOI-1231 b is an excellent target for atmospheric characterization. With a few transit observations, it will be possible to detect spectral features in an atmosphere similar to that of K2-18 b ([Benneke et al. 2019b](#); [Tsiaras et al. 2019](#)), enabling the first comparative planetology in the temperature range 250 – 350 Kelvin.

5.2. Prospects for JWST Observations

With just one transit observed with *JWST*’s NIRISS, for a clear, solar composition atmosphere, we expect to detect TOI-1231 b’s spectrum (dominated by water at NIRISS wavelengths) with 90σ significance ([Kempton et al. 2018](#)).

We also investigate prospects for a cloudy atmosphere, using PLATON ([Zhang et al. 2019](#)) to generate a solar composition model spectrum with a cloud deck pressure of 10 mbar (similar to GJ 3470 b; [Benneke et al. 2019a](#)). We then used PandEXO ([Batalha et al. 2017](#)) to simulate a transmission spectrum for such an atmosphere. We find that even in this scenario, one transit with the NIRISS instrument would be sufficient to detect water absorption with 7.5σ significance. For reference, this is 2σ higher than the detection significance obtained with six HST WFC3 transits for GJ 3470b ([Benneke et al.](#)

2019a), a planet with a similar size but much lower density (and also orbiting a $0.5 R_{\odot}$ star).

5.3. Probing Atmospheric Escape

Given TOI-1231 b’s low gravitational potential and expected XUV instellation, we consider the likelihood that atmospheric escape is occurring and traceable with H I Lyman α ($\text{Ly}\alpha$; 1216 \AA) and the meta-stable He I line (10830 \AA). TOI-1231 b’s bulk density is similar to that of GJ 436 b ($1.80 \pm 0.29 \text{ g cm}^{-3}$; Maciejewski et al. 2014), a planet well known for its vigorously escaping atmosphere (Kulow et al. 2014; Ehrenreich et al. 2015). TOI-1231’s fundamental stellar properties are very similar to GJ 436’s, and our PFS spectra indicate that TOI-1231’s $\log_{10} R'_{HK} = -5.06$ is nearly equivalent to GJ 436’s (-5.09 ; Boro Saikia et al. 2018), indicating the same level of magnetic activity. Since R'_{HK} is known to correlate well with UV emission (Youngblood et al. 2017), we assume GJ 436’s synthetic X-ray and UV spectrum from Peacock et al. (2019) as a proxy for TOI-1231’s. The integrated flux from $100\text{-}912 \text{ \AA}$ at 0.13 au is $172 \text{ erg cm}^{-2} \text{ s}^{-1}$, but could be as low as $\sim 53 \text{ erg cm}^{-2} \text{ s}^{-1}$ according to the estimates from the MUSCLES Treasury Survey (France et al. 2016; Youngblood et al. 2016; Loyd et al. 2016) based on Linsky et al. (2014). In the energy-limited approximation (Salz et al. 2016), the mass loss rate scales inversely with the planet’s bulk density and inversely with the square of the orbital distance. Thus, under this approximation we expect a mass loss rate about 14 times lower for TOI-1231 b than for GJ 436 b.

To better understand the properties of the escaping atmosphere of TOI-1231 b, we constructed a 1D model of this planet’s upper atmosphere, which solves the hydrodynamics equations for an escaping atmosphere and considers photochemistry at pressures $\lesssim 1 \mu\text{bar}$, and radial distances from the planet center $r/R_p = 1\text{-}10$. We assume the planet’s bulk composition is dominated by H_2 and He, and set volume mixing ratios at the $1 \mu\text{bar}$ boundary of 0.9 for H_2 and 0.1 for He. The model is one-dimensional and spherically-symmetric, appropriate to the sub-stellar line. See García Muñoz et al. (2020) and references within for more details about the method. The model simulations shown in Figure 8 are specific to the stellar spectrum from Peacock et al. (2019) and assume supersonic conditions at $r/R_p \sim 10$. We take the stellar spectrum in its original format¹⁶, correcting only for orbital distance. A one-dimensional approach is expected to give a good representation of the flow within a few planetary radii from the surface, but cannot capture the shape of the flow after its interaction with the stel-

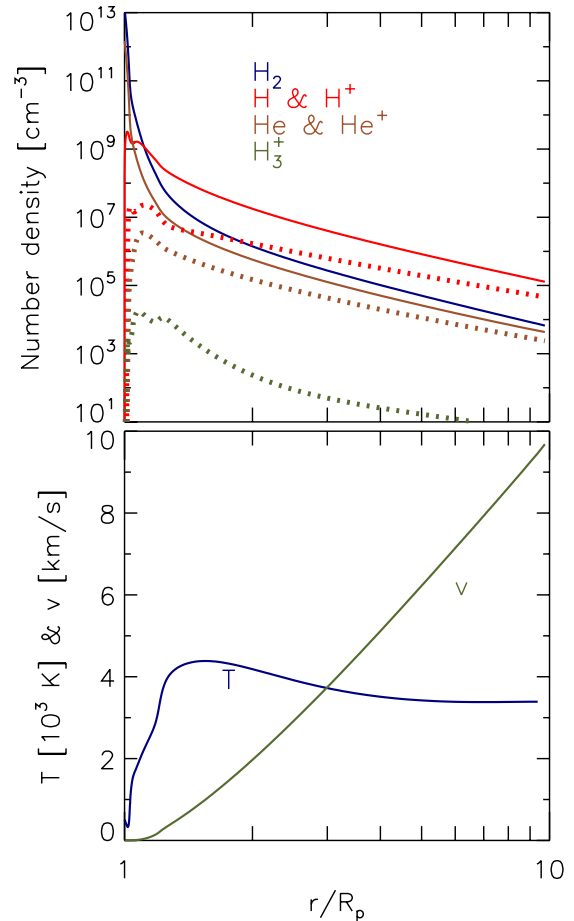


Figure 8. Results from the simulated upper atmosphere of TOI-1231 b. Top panel: the number density of H_2 (blue), H and H^+ (red), He and He^+ (brown), and H_3^+ (green) are shown as a function of distance (r/R_p) from the planet’s $1\text{-}\mu\text{m}$ pressure level, that we approximate as the planet’s optical radius (R_p). Neutrals are shown as solid lines and ions are shown as dotted lines. Bottom panel: The temperature (10^3 K ; blue line) and outward bulk velocity (km s^{-1} ; green line) are shown as a function of distance from the planet’s $1\text{-}\mu\text{m}$ pressure level.

lar wind. In any case, our predictions provide helpful insight to understand the prevalent forms of hydrogen, and the range of temperatures and velocities expected in the vicinity of the planet.

Figure 8 shows that H_2 remains abundant up to very high altitudes, and that the transition from H to H^+ also occurs at high altitude, a condition favorable for $\text{Ly}\alpha$ transit spectroscopy. Unlike for typical hot Jupiters, H_3^+ remains relatively abundant over an extended column and contributes to cooling of the atmosphere and to reducing the mass loss rate. The model predicts that the planet is losing $2.3 \times 10^9 \text{ gs}^{-1}$ (integrated over a solid angle 4π).

¹⁶ <http://archive.stsci.edu/hlsp/hazmat>

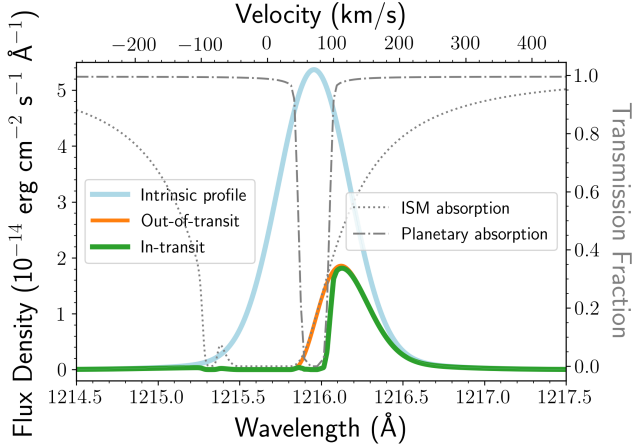


Figure 9. The flux densities of TOI-1231 at Earth without (blue) and with (orange) ISM attenuation and with ISM and in-transit planetary absorption (green). TOI-1231’s intrinsic Ly α profile is scaled from GJ 436’s and shifted to $+70.5 \text{ km s}^{-1}$, and the ISM attenuation is conservatively assumed to be $\log N(\text{HI}) = 18.6$, centered at -4 km s^{-1} (Redfield & Linsky 2008). The planetary absorption during transit is centered at 0 km s^{-1} in the stellar rest frame. The dotted and dash-dotted grey lines represent the ISM and in-transit planetary absorption, respectively (right axis). The transmission fraction ($e^{-\tau}$) is unity where all photons are transmitted and zero where all photons are absorbed.

We use the H I profile predicted by the model to estimate the Ly α transit depth attributable to hydrogen escaping the planet and before interacting with the stellar wind. This ‘cold’ component is typically hidden by ISM absorption and has so far remained undetected. The Ly α absorption reported in other systems including GJ 436 b (e.g., Ehrenreich et al. 2015) is attributed to a ‘hot’ component that results from charge exchange of the hydrogen atoms from the planet and the stellar wind protons (Khodachenko et al. 2019).

Despite the smaller expected escape rate with respect to other planets, TOI-1231 b’s exosphere may be observable during a H I Ly α (1215.67 \AA) transit. The host star’s radial velocity ($+70.5 \text{ km s}^{-1}$) Doppler shifts the entire system partially out of the bulk of ISM’s H I attenuation region, allowing access to the core of the Ly α line and therefore to the ‘cold’ component.

In order to assess the utility of a Ly α transit with HST for studying this planet, we estimate the profiles of the stellar Ly α emission, ISM attenuation, and planetary absorption (Figure 9). We use the reconstructed Ly α profile of GJ 436 (Youngblood et al. 2016) rescaled to match TOI-1231’s distance. For the ISM, we assume a velocity centroid for the H I absorbers of -4.3 km s^{-1} based on a kinematic model for the local ISM (Redfield & Linsky 2008) and a conservative H I column density

$\log_{10} N(\text{HI}) = 18.6$ based on measured column densities of nearby sight lines (Wood et al. 2005; Youngblood et al. 2016; Waalkes et al. 2019). Using STScI’s online exposure time calculator for STIS with the G140M, 1222 central wavelength, and $52'' \times 0.2''$ slit, we find that the expected planetary absorption around the Ly α line core (the ‘cold’ component) could be detected at high confidence in a single transit.

We have not modeled the expected transit signature for metastable He I, but note the potential for exploring this planet’s upper atmosphere with He I transits. However, as noted above TOI-1231’s XUV spectrum, which is responsible for both driving escape and populating the metastable He I state, is likely very similar to GJ 436’s, and GJ 436 b’s vigorously escaping atmosphere was not detected in He I (Nortmann et al. 2018). TOI-1231 b’s larger orbit ($a = 0.1266 \text{ AU}$) further lowers its likelihood to be a promising He I target, as the furthest planet with a confirmed He I detection thus far is WASP 107 b which has a semi-major axis of only 0.055 au and orbits a more favorable (to He I excitation) K6V star (Spake et al. 2018). See Oklopčić & Hirata (2018) and Oklopčić (2019) for more details on the prospects tracing atmospheric escape with metastable He I.

6. CONCLUSIONS

We reported the *TESS* discovery and confirmation (using several ground-based facilities) of TOI 1231 b, a temperate, Neptune-sized planet orbiting a nearby (27.6 pc) M dwarf star. The mass and radius of TOI-1231 b were measured to be $15.5 \pm 3.3 M_{\oplus}$ and $3.65^{+0.16}_{-0.15} R_{\oplus}$, respectively. By virtue of its volatile rich atmosphere, long transit duration and small host star, TOI 1231 b appears to be one of the most promising small exoplanets for transmission spectroscopy with HST and *JWST* detected by the *TESS* mission thus far. It represents a rare and valuable addition to the current sample of just one other low-density Neptune-sized or smaller planet with an equilibrium temperature in the $250\text{-}350 \text{ K}$ range and a transmission spectrum (K2-18 b). Moreover, its high systemic radial velocity makes it a particularly attractive target for atmospheric escape observations via the H I Lyman α , and possibly the meta-stable He I line.

This planet also serves as excellent motivation for follow up efforts focused on *TESS* single transit events (Villanueva et al. 2019), which is how TOI-1231 b would have presented itself if the host star was only observed for a single *TESS* sector.

Table 3. Median values and 68% confidence interval for EXOFASTv2 results on TOI-1231.

Notes from Eastman et al. (2019): The optimal conjunction time (T_0) is the time of conjunction that minimizes the covariance with the planet’s period and therefore has the smallest uncertainty. The equilibrium temperature of the planet (T_{eq}) is calculated using Equation 1 of Hansen & Barman (2007) and assumes no albedo and perfect heat redistribution. The tidal circularization timescale (τ_{circ}) is calculated using Equation 3 from Adams & Laughlin (2006) and assumes $Q = 10^6$. The $3.6\mu\text{m}$ and $4.6\mu\text{m}$ secondary occultation depths use a black-body approximation of the stellar flux, F_* , at T_{eff} and of the planetary flux, F_p , at T_{eq} and are calculated using $\delta_{S,\lambda} = \frac{(R_p/R_*)^2}{(R_p/R_*)^2 + (F_*/F_p)}$.

Parameter	Units	Values
EXOFASTv2 Gaussian priors:		
M_*	Stellar mass (M_\odot)	0.485 ± 0.024
T_{eff}	Effective Temperature (K)	3562 ± 101
[Fe/H] ...	Metallicity (dex)	0.05 ± 0.08
ϖ	Parallax (mas)	36.3726 ± 0.0163
A_V	V-band extinction (mag)	0.0031 ± 0.0465
Stellar Parameters:		
M_*	Mass (M_\odot)	0.485 ± 0.024
R_*	Radius (R_\odot)	$0.476^{+0.015}_{-0.014}$
$R_{*,SED}$..	Radius ¹ (R_\odot)	0.4766 ± 0.0084
L_*	Luminosity (L_\odot)	0.0326 ± 0.0010
F_{Bol}	Bolometric Flux (10^{-9} erg s ⁻¹ cm ⁻²)	$1.381^{+0.043}_{-0.044}$
ρ_*	Density (g cm ⁻³)	$6.31^{+0.68}_{-0.64}$
$\log g$	Surface gravity (log(cm s ⁻²))	$4.767^{+0.033}_{-0.035}$
T_{eff}	Effective Temperature (K)	3553^{+51}_{-52}
$T_{eff,SED}$..	Effective Temperature ¹ (K)	3553 ± 31
[Fe/H] ...	Metallicity (dex)	$0.041^{+0.069}_{-0.063}$
A_V	V-band extinction (mag)	$0.030^{+0.033}_{-0.021}$
σ_{SED}	SED photometry error scaling	$2.09^{+0.52}_{-0.37}$
ϖ	Parallax (mas)	36.373 ± 0.016
d	Distance (pc)	27.493 ± 0.012
Planetary Parameters:		
		b
P	Period (days)	$24.245586^{+0.000064}_{-0.000066}$
R_P	Radius (R_E)	$3.65^{+0.16}_{-0.15}$
M_P	Mass (M_E)	15.4 ± 3.3
T_C	Time of conjunction (BJD _{TDB})	$2458563.88838^{+0.00057}_{-0.00058}$
T_T	Time of minimum projected separation (BJD _{TDB})	$2458563.88839^{+0.00057}_{-0.00058}$
T_0	Optimal conjunction Time (BJD _{TDB})	$2458685.11630^{+0.00048}_{-0.00049}$
a	Semi-major axis (AU)	$0.1288^{+0.0021}_{-0.0022}$

Table 3 continued

Table 3 (continued)

Parameter	Units	Values
i	Inclination (Degrees).....	89.73 ± 0.18
e	Eccentricity	$0.087^{+0.12}_{-0.061}$
ω_*	Argument of Periastron (Degrees).....	176^{+81}_{-90}
T_{eq}	Equilibrium temperature (K).....	$329.6^{+3.8}_{-3.7}$
τ_{circ}	Tidal circularization timescale (Gyr).....	20600^{+9500}_{-8600}
K	RV semi-amplitude (m s^{-1}).....	5.6 ± 1.2
R_P/R_* ..	Radius of planet in stellar radii	$0.0701^{+0.0019}_{-0.0017}$
a/R_*	Semi-major axis in stellar radii	58.1 ± 2.0
δ	Transit depth (fraction).....	$0.00492^{+0.00027}_{-0.00024}$
$Depth$...	Flux decrement at mid transit	$0.00492^{+0.00027}_{-0.00024}$
τ	Ingress/egress transit duration (days).....	$0.00946^{+0.0018}_{-0.00066}$
T_{14}	Total transit duration (days).....	$0.1350^{+0.0017}_{-0.0014}$
T_{FWHM} ..	FWHM transit duration (days).....	0.1251 ± 0.0013
b	Transit Impact parameter	$0.27^{+0.19}_{-0.18}$
b_S	Eclipse impact parameter	$0.27^{+0.14}_{-0.18}$
τ_S	Ingress/egress eclipse duration (days).....	$0.00961^{+0.00085}_{-0.00077}$
$T_{S,14}$	Total eclipse duration (days).....	$0.136^{+0.012}_{-0.013}$
$T_{S,FWHM}$	FWHM eclipse duration (days).....	$0.126^{+0.012}_{-0.013}$
$\delta_{S,2.5\mu m}$..	Blackbody eclipse depth at $2.5\mu m$ (ppm).....	$0.000522^{+0.00012}_{-0.000097}$
$\delta_{S,5.0\mu m}$..	Blackbody eclipse depth at $5.0\mu m$ (ppm).....	$0.99^{+0.13}_{-0.11}$
$\delta_{S,7.5\mu m}$..	Blackbody eclipse depth at $7.5\mu m$ (ppm).....	$10.49^{+1.0}_{-0.86}$
ρ_P	Density (g cm^{-3}).....	$1.74^{+0.47}_{-0.42}$
$\log g_P$	Surface gravity	$3.054^{+0.094}_{-0.11}$
Θ	Safronov Number	0.079 ± 0.017
$\langle F \rangle$	Incident Flux ($10^9 \text{ erg s}^{-1} \text{ cm}^{-2}$).....	$0.00263^{+0.00013}_{-0.00014}$
T_P	Time of Periastron (BJD_{TDB}).....	$2458543.7^{+4.8}_{-6.3}$
T_S	Time of eclipse (BJD_{TDB}).....	$2458575.45^{+0.95}_{-2.3}$
T_A	Time of Ascending Node (BJD_{TDB}).....	$2458557.57^{+0.57}_{-1.4}$
T_D	Time of Descending Node (BJD_{TDB}).....	$2458569.62^{+0.63}_{-1.1}$
V_c/V_e	$0.993^{+0.062}_{-0.048}$
$e \cos \omega_*$	$-0.036^{+0.061}_{-0.15}$
$e \sin \omega_*$	$0.002^{+0.046}_{-0.066}$
$M_P \sin i$..	Minimum mass (M_E).....	15.4 ± 3.3
M_P/M_* ..	Mass ratio	$0.000096^{+0.000021}_{-0.000020}$
d/R_*	Separation at mid transit	$57.5^{+4.3}_{-4.4}$
P_T	A priori non-grazing transit prob	$0.0162^{+0.0014}_{-0.0011}$
$P_{T,G}$	A priori transit prob	$0.0186^{+0.0016}_{-0.0013}$
P_S	A priori non-grazing eclipse prob	$0.01607^{+0.0016}_{-0.00069}$
$P_{S,G}$	A priori eclipse prob	$0.01849^{+0.0019}_{-0.00080}$

Wavelength Parameters:

R

z'

TESS

Table 3 continued

Table 3 (continued)

Parameter	Units	Values		
u_1	linear limb-darkening coeff	$0.31^{+0.33}_{-0.22}$	$0.20^{+0.25}_{-0.15}$	0.31 ± 0.19
u_2	quadratic limb-darkening coeff	$0.36^{+0.33}_{-0.44}$	$0.22^{+0.34}_{-0.27}$	$0.07^{+0.29}_{-0.23}$
A_D	Dilution from neighboring stars	–	–	$-0.001^{+0.046}_{-0.049}$
Telescope Parameters:		PFS velocities		
γ_{rel}	Relative RV Offset (m/s)	0.11 ± 0.91		
σ_J	RV Jitter (m/s)	$3.03^{+1.0}_{-0.72}$		
σ_J^2	RV Jitter Variance	$9.2^{+7.2}_{-3.8}$		

¹This value ignores the systematic error and is for reference only

This paper includes data collected by the *TESS* mission. Funding for the *TESS* mission is provided by NASA’s Science Mission directorate. We acknowledge the use of public *TESS* Alert data from pipelines at the *TESS* Science Office and the *TESS* Science Operations Center. This paper includes data gathered with the 6.5 meter Magellan Telescopes located at Las Campanas Observatory, Chile. This work makes use of observations from the LCOGT network and from the ASTEP telescope. ASTEP benefited from the support of the French and Italian polar agencies IPEV and PNRA in the framework of the Concordia station program. This work has made use of data from the European Space Agency (ESA) mission Gaia (<https://www.cosmos.esa.int/gaia>), processed by the Gaia Data Processing and Analysis Consortium (DPAC, <https://www.cosmos.esa.int/web/gaia/dpac/consortium>). Funding for the DPAC has been provided by national institutions, in particular the institutions participating in the Gaia Multilateral Agreement. Some of the observations in the paper made use of the High-Resolution Imaging instrument Zorro. Zorro was funded by the NASA Exoplanet Exploration Program and built at the NASA Ames Research Center by Steve B. Howell, Nic Scott, Elliott P. Horch, and Emmett Quigley. Zorro was mounted on the Gemini South telescope of the international Gemini Observatory, a program of NSF’s OIR Lab, which is managed by the Association of Universities for Research in Astronomy (AURA) under a cooperative agreement with the National Science Foundation on behalf of the Gemini partnership: the National Science Foundation (United States), National Research Council (Canada), Agencia Nacional de Investigación y Desarrollo (Chile), Ministerio de Ciencia, Tecnología e Innovación (Argentina), Ministério da Ciência, Tec-

nologia, Inovações e Comunicações (Brazil), and Korea Astronomy and Space Science Institute (Republic of Korea). Resources supporting this work were provided by the NASA High-End Computing (HEC) Program through the NASA Advanced Supercomputing (NAS) Division at Ames Research Center for the production of the SPOC data products. Some of the data presented in this paper were obtained from the Mikulski Archive for Space Telescopes (MAST). Support for MAST for non-HST data is provided by the NASA Office of Space Science via grant NNX13AC07G and by other grants and contracts. This research has made use of the NASA Exoplanet Archive, which is operated by the California Institute of Technology, under contract with the National Aeronautics and Space Administration under the Exoplanet Exploration Program. This research has made use of NASA’s Astrophysics Data System. This research has also made use of the Exoplanet Follow-up Observation Program website, which is operated by the California Institute of Technology, under contract with the National Aeronautics and Space Administration under the Exoplanet Exploration Program. This research made use of Astropy, a community-developed core Python package for Astronomy ([Astropy Collaboration et al. 2013](#)). Part of this research was carried out at the Jet Propulsion Laboratory, California Institute of Technology, under a contract with the National Aeronautics and Space Administration (NASA). D. D. acknowledges support from the TESS Guest Investigator Program grant 80NSSC19K1727 and NASA Exoplanet Research Program grant 18-2XRP18.2-0136. TD acknowledges support from MIT’s Kavli Institute as a Kavli postdoctoral fellow. E.M. acknowledges support from NASA award 17-K2G06-0030. P.M. acknowledges support from the European Research Council under the European Union’s Horizon 2020 research and innovation program under grant agreement No. 832428. T.G.,

A.A., L.A., D.M., F.-X.S. acknowledge support from Idex UCAJEDI (ANR-15-IDEX-01). D.J.S. acknowledges funding support from the Eberly Research Fellowship from The Pennsylvania State University Eberly College of Science. The Center for Exoplanets and Habitable Worlds is supported by the Pennsylvania State University, the Eberly College of Science, and the Pennsylvania Space Grant Consortium. This research received funding from the European Research Council (ERC) under the European Union’s Horizon 2020 research and innovation programme (grant agreement n° 803193/BEBOP), and from the Science and Technology Facilities Council (STFC; grant n° ST/S00193X/1). This publication makes use of VOSA, developed under

the Spanish Virtual Observatory project supported by the Spanish MINECO through grant AyA2017-84089. VOSA has been partially updated by using funding from the European Union’s Horizon 2020 Research and Innovation Programme, under Grant Agreement n° 776403 (EXOPLANETS-A).

Facilities: TESS, Magellan:Clay (Planet Finder Spectrograph), Gemini-South (Zorro), SOAR, LCOGT, ASTEP

Software: AstroImageJ (Collins et al. 2017), TAPIR (Jensen 2013), EXOFASTv2 (Eastman et al. 2019), petitCODE (Mollière et al. 2017), PyMultiNest (Buchner 2014), MultiNest (Feroz et al. 2009), Astropy (Astropy Collaboration et al. 2013)

REFERENCES

- 1997, ESA Special Publication, Vol. 1200, The HIPPARCOS and TYCHO catalogues. Astrometric and photometric star catalogues derived from the ESA HIPPARCOS Space Astrometry Mission
- Adams, F. C., & Laughlin, G. 2006, *ApJ*, 649, 1004
- Anders, F., Khalatyan, A., Chiappini, C., et al. 2019, *A&A*, 628, A94
- Astropy Collaboration, Robitaille, T. P., Tollerud, E. J., et al. 2013, *A&A*, 558, A33
- Barclay, T., Pepper, J., & Quintana, E. V. 2018, *ApJS*, 239, 2
- Batalha, N. E., Lewis, T., Fortney, J. J., et al. 2019, *ApJL*, 885, L25
- Batalha, N. E., Mandell, A., Pontoppidan, K., et al. 2017, *PASP*, 129, 064501
- Bayo, A., Rodrigo, C., Barrado Y Navascués, D., et al. 2008, *A&A*, 492, 277
- Benneke, B., & Seager, S. 2013, *ApJ*, 778, 153
- Benneke, B., Knutson, H. A., Lothringer, J., et al. 2019a, *Nature Astronomy*, 3, 813
- Benneke, B., Wong, I., Piaulet, C., et al. 2019b, *ApJL*, 887, L14
- Bensby, T., Feltzing, S., & Oey, M. S. 2014, *A&A*, 562, A71
- Bonfils, X., Almenara, J. M., Jocou, L., et al. 2015, in *Society of Photo-Optical Instrumentation Engineers (SPIE) Conference Series*, Vol. 9605, *Techniques and Instrumentation for Detection of Exoplanets VII*, 96051L
- Boro Saikia, S., Marvin, C. J., Jeffers, S. V., et al. 2018, *A&A*, 616, A108
- Brown, T. M., Baliber, N., Bianco, F. B., et al. 2013, *Publications of the Astronomical Society of the Pacific*, 125, 1031
- Buchner, J. 2014, arXiv e-prints, arXiv:1407.5459
- Buchner, J., Georgakakis, A., Nandra, K., et al. 2014, *A&A*, 564, A125
- Burt, J. A., Nielsen, L. D., Quinn, S. N., et al. 2020, *AJ*, 160, 153
- Butler, R. P., Marcy, G. W., Williams, E., et al. 1996, *PASP*, 108, 500
- Cameron, A. C. 2012, *Nature*, 492, 48
- Casagrande, L., Flynn, C., & Bessell, M. 2008, *MNRAS*, 389, 585
- Collins, K. A., Kielkopf, J. F., Stassun, K. G., & Hessman, F. V. 2017, *AJ*, 153, 77
- Crane, J. D., Shectman, S. A., & Butler, R. P. 2006, *Society of Photo-Optical Instrumentation Engineers (SPIE) Conference Series*, Vol. 6269, *The Carnegie Planet Finder Spectrograph*, 62693I
- Crane, J. D., Shectman, S. A., Butler, R. P., et al. 2010, in *Society of Photo-Optical Instrumentation Engineers (SPIE) Conference Series*, Vol. 7735, *Proc. SPIE*, 773553
- Crane, J. D., Shectman, S. A., Butler, R. P., Thompson, I. B., & Burley, G. S. 2008, *Society of Photo-Optical Instrumentation Engineers (SPIE) Conference Series*, Vol. 7014, *The Carnegie Planet Finder Spectrograph: a status report*, 701479
- Crossfield, I. J. M., & Kreidberg, L. 2017, *AJ*, 154, 261
- Cutri, R. M., Skrutskie, M. F., van Dyk, S., et al. 2003, *VizieR Online Data Catalog*, II/246
- Cutri, R. M., Wright, E. L., Conrow, T., et al. 2012, *Explanatory Supplement to the WISE All-Sky Data Release Products*, Tech. rep.
- Dehnen, W. 2000, *AJ*, 119, 800
- Dragomir, D., Teske, J., Günther, M. N., et al. 2019, *ApJL*, 875, L7
- Eastman, J., Gaudi, B. S., & Agol, E. 2013, *PASP*, 125, 83

- Eastman, J. D., Rodriguez, J. E., Agol, E., et al. 2019, arXiv e-prints, arXiv:1907.09480
- Ehrenreich, D., Bourrier, V., Wheatley, P. J., et al. 2015, *Nature*, 522, 459
- Espinoza, N., Kossakowski, D., & Brahm, R. 2019, *MNRAS*, 490, 2262
- Feroz, F., Hobson, M. P., & Bridges, M. 2009, *MNRAS*, 398, 1601
- Foreman-Mackey, D., Agol, E., Ambikasaran, S., & Angus, R. 2017, *AJ*, 154, 220
- France, K., Loyd, R. O. P., Youngblood, A., et al. 2016, *ApJ*, 820, 89
- Frith, J., Pinfield, D. J., Jones, H. R. A., et al. 2013, *MNRAS*, 435, 2161
- Gagné, J., Mamajek, E. E., Malo, L., et al. 2018, *ApJ*, 856, 23
- Gaia Collaboration, Brown, A. G. A., Vallenari, A., et al. 2018, *A&A*, 616, A1
- Gaidos, E., Mann, A. W., Lépine, S., et al. 2014, *MNRAS*, 443, 2561
- García Muñoz, A., Youngblood, A., Fossati, L., et al. 2020, *ApJL*, 888, L21
- Guerrero, N. M., Seager, S., Huang, C. X., et al. 2021, arXiv e-prints, arXiv:2103.12538
- Guillot, T., Abe, L., Agabi, A., et al. 2015, *Astronomische Nachrichten*, 336, 638
- Guo, X., Crossfield, I. J. M., Dragomir, D., et al. 2020, *AJ*, 159, 239
- Hansen, B. M. S., & Barman, T. 2007, *ApJ*, 671, 861
- Henden, A. A., Templeton, M., Terrell, D., et al. 2016, *VizieR Online Data Catalog*, II/336
- Howell, S. B., Everett, M. E., Sherry, W., Horch, E., & Ciardi, D. R. 2011, *AJ*, 142, 19
- Huang, C. X., Burt, J., Vanderburg, A., et al. 2018, *ApJL*, 868, L39
- Jenkins, J. M., Twicken, J. D., McCauliff, S., et al. 2016a, *Society of Photo-Optical Instrumentation Engineers (SPIE) Conference Series*, Vol. 9913, The TESS science processing operations center, 99133E
- Jenkins, J. M., Twicken, J. D., McCauliff, S., et al. 2016b, in *Proc. SPIE*, Vol. 9913, Software and Cyberinfrastructure for Astronomy IV, 99133E
- Jensen, E. 2013, *Tapir: A web interface for transit/eclipse observability*, *Astrophysics Source Code Library*, ascl:1306.007
- Jiang, J. H., Ji, X., Cowan, N., Hu, R., & Zhu, Z. 2019, *AJ*, 158, 96
- Johnson, J. A., & Apps, K. 2009, *ApJ*, 699, 933
- Kass, R. E., & Raftery, A. E. 1995, *Journal of the American Statistical Association*, 90, 773
- Kempton, E. M.-R., Bean, J. L., Louie, D. R., et al. 2018, *PASP*, 130, 114401
- Khodachenko, M. L., Shaikhislamov, I. F., Lammer, H., et al. 2019, *ApJ*, 885, 67
- Kirkpatrick, J. D., Schneider, A., Fajardo-Acosta, S., et al. 2014, *ApJ*, 783, 122
- Kraus, A. L., & Hillenbrand, L. A. 2012, *ApJ*, 757, 141
- Kreidberg, L. 2015, *PASP*, 127, 1161
- Kulow, J. R., France, K., Linsky, J., & Parke Loyd, R. O. 2014, *The Astrophysical Journal*, 786, 132
- Kurucz, R. L. 2005, *Memorie della Societa Astronomica Italiana Supplementi*, 8, 14
- Lallement, R., Capitanio, L., Ruiz-Dern, L., et al. 2018, *A&A*, 616, A132
- Lépine, S., & Gaidos, E. 2011, *AJ*, 142, 138
- Li, J., Tenenbaum, P., Twicken, J. D., et al. 2019, *PASP*, 131, 024506
- Lindgren, L., Klioner, S. A., Hernández, J., et al. 2020, arXiv e-prints, arXiv:2012.03380
- Linsky, J. L., Fontenla, J., & France, K. 2014, *The Astrophysical Journal*, 780, 61
- Loyd, R. O. P., France, K., Youngblood, A., et al. 2016, *ApJ*, 824, 102
- Lucy, L. B., & Sweeney, M. A. 1971, *AJ*, 76, 544
- Luque, R., Pallé, E., Kossakowski, D., et al. 2019, *A&A*, 628, A39
- Luyten, W. J. 1957, A catalogue of 9867 stars in the Southern Hemisphere with proper motions exceeding 0."2 annually.
- . 1979, *New Luyten catalogue of stars with proper motions larger than two tenths of an arcsecond; and first supplement; NLTT. (Minneapolis (1979))*
- Maciejewski, G., Niedzielski, A., Nowak, G., et al. 2014, *AcA*, 64, 323
- Mackereth, J. T., & Bovy, J. 2018, *PASP*, 130, 114501
- Mamajek, E. E., Bartlett, J. L., Seifahrt, A., et al. 2013, *AJ*, 146, 154
- Mann, A. W., Feiden, G. A., Gaidos, E., Boyajian, T., & von Braun, K. 2015, *ApJ*, 804, 64
- Mann, A. W., Dupuy, T., Kraus, A. L., et al. 2019, *ApJ*, 871, 63
- Marcy, G. W., & Butler, R. P. 1992, *PASP*, 104, 270
- Mékarnia, D., Guillot, T., Rivet, J. P., et al. 2016, *MNRAS*, 463, 45
- Mollière, P., van Boekel, R., Bouwman, J., et al. 2017, *A&A*, 600, A10
- Mollière, P., Wardenier, J. P., van Boekel, R., et al. 2019, *A&A*, 627, A67
- Monari, G., Famaey, B., Siebert, A., Wegg, C., & Gerhard, O. 2019, *A&A*, 626, A41

- Morley, C. V., Fortney, J. J., Kempton, E. M. R., et al. 2013, *ApJ*, 775, 33
- Morley, C. V., Marley, M. S., Fortney, J. J., et al. 2014, *ApJ*, 787, 78
- Morris, R. L., Twicken, J. D., Smith, J. C., et al. 2017, *Kepler Data Processing Handbook: Photometric Analysis*, Tech. rep.
- Muirhead, P. S., Dressing, C. D., Mann, A. W., et al. 2018, *AJ*, 155, 180
- Nave, G. 2017, in *ESO Calibration Workshop: The Second Generation VLT Instruments and Friends*, 32
- Nortmann, L., Pallé, E., Salz, M., et al. 2018, *Science*, 362, 1388
- Oklopčić, A. 2019, *ApJ*, 881, 133
- Oklopčić, A., & Hirata, C. M. 2018, *ApJL*, 855, L11
- Peacock, S., Barman, T., Shkolnik, E. L., et al. 2019, *The Astrophysical Journal*, 886, 77
- Redfield, S., & Linsky, J. L. 2008, *The Astrophysical Journal*, 673, 283
- Reiners, A., Joshi, N., & Goldman, B. 2012, *AJ*, 143, 93
- Ricker, G. R., Winn, J. N., Vanderspek, R., et al. 2014, in *Society of Photo-Optical Instrumentation Engineers (SPIE) Conference Series*, Vol. 9143, *Proc. SPIE*, 914320
- Robertson, P., Endl, M., Cochran, W. D., & Dodson-Robinson, S. E. 2013, *ApJ*, 764, 3
- Robertson, P., Stefansson, G., Mahadevan, S., et al. 2020, *ApJ*, 897, 125
- Rodriguez, J. E., Quinn, S. N., Huang, C. X., et al. 2019, *AJ*, 157, 191
- Saar, S. H., & Donahue, R. A. 1997, *ApJ*, 485, 319
- Salz, M., Schneider, P. C., Czesla, S., & Schmitt, J. H. M. M. 2016, *A&A*, 585, L2
- Saumon, D., & Marley, M. S. 2008, *ApJ*, 689, 1327
- Schlaufman, K. C., & Laughlin, G. 2010, *A&A*, 519, A105
- Schneider, A. C., Greco, J., Cushing, M. C., et al. 2016, *ApJ*, 817, 112
- Schönrich, R., Binney, J., & Dehnen, W. 2010, *MNRAS*, 403, 1829
- Skrutskie, M. F., Cutri, R. M., Stiening, R., et al. 2006, *AJ*, 131, 1163
- Smith, J. C., Stumpe, M. C., Van Cleve, J. E., et al. 2012, *PASP*, 124, 1000
- Spake, J. J., Sing, D. K., Evans, T. M., et al. 2018, *Nature*, 557, 68
- Speagle, J. S. 2020, *MNRAS*, 493, 3132
- Stassun, K. G., Collins, K. A., & Gaudi, B. S. 2017, *AJ*, 153, 136
- Stassun, K. G., Corsaro, E., Pepper, J. A., & Gaudi, B. S. 2018, *AJ*, 155, 22
- Stassun, K. G., & Torres, G. 2016, *AJ*, 152, 180
- Stassun, K. G., Oelkers, R. J., Paegert, M., et al. 2019, *AJ*, 158, 138
- Stumpe, M. C., Smith, J. C., Catanzarite, J. H., et al. 2014, *PASP*, 126, 100
- Stumpe, M. C., Smith, J. C., Van Cleve, J. E., et al. 2012, *PASP*, 124, 985
- Sullivan, P. W., Winn, J. N., Berta-Thompson, Z. K., et al. 2015, *ApJ*, 809, 77
- Tokovinin, A., Mason, B. D., Hartkopf, W. I., Mendez, R. A., & Horch, E. P. 2018, *AJ*, 155, 235
- Torres, S., Cai, M. X., Brown, A. G. A., & Portegies Zwart, S. 2019, *A&A*, 629, A139
- Tsiaras, A., Waldmann, I. P., Tinetti, G., Tennyson, J., & Yurchenko, S. N. 2019, *Nature Astronomy*, 3, 1086
- Twicken, J. D., Clarke, B. D., Bryson, S. T., et al. 2010, *Society of Photo-Optical Instrumentation Engineers (SPIE) Conference Series*, Vol. 7740, *Photometric analysis in the Kepler Science Operations Center pipeline*, 774023
- Twicken, J. D., Catanzarite, J. H., Clarke, B. D., et al. 2018, *PASP*, 130, 064502
- van Leeuwen, F., de Bruijne, J., Babusiaux, C., et al. 2021, *Gaia EDR3 documentation*, *Gaia EDR3 documentation*
- Vanderspek, R., Huang, C. X., Vanderburg, A., et al. 2019, *ApJL*, 871, L24
- Villanueva, Jr., S., Dragomir, D., & Gaudi, B. S. 2019, *AJ*, 157, 84
- Waalkes, W. C., Berta-Thompson, Z., Bourrier, V., et al. 2019, *The Astronomical Journal*, 158, 50
- Wang, S., Jones, M., Shporer, A., et al. 2019, *AJ*, 157, 51
- Wood, B. E., Redfield, S., Linsky, J. L., Muller, H., & Zank, G. P. 2005, *The Astrophysical Journal Supplement Series*, 159, 118
- Youngblood, A., France, K., Loyd, R., et al. 2016, *Astrophysical Journal*, 824, doi:10.3847/0004-637X/824/2/101
- Youngblood, A., France, K., Loyd, R. O. P., et al. 2017, *ApJ*, 843, 31
- Zhang, M., Chachan, Y., Kempton, E. M. R., & Knutson, H. A. 2019, *PASP*, 131, 034501
- Ziegler, C., Tokovinin, A., Briceño, C., et al. 2020, *AJ*, 159, 19